Non-Markovian recovery makes complex networks more resilient against large-scale failures

Zhao-Hua Lin[1], Mi Feng [2], Ming Tang [1,2✉], Zonghua Liu[1✉], Chen Xu[3], Pak Ming Hui [4] & Ying-Cheng Lai [5]

Non-Markovian spontaneous recovery processes with a time delay (memory) are ubiquitous in the real world. How does the non-Markovian characteristic affect failure propagation in complex networks? We consider failures due to internal causes at the nodal level and external failures due to an adverse environment, and develop a pair approximation analysis taking into account the two-node correlation. In general, a high failure stationary state can arise, corresponding to large-scale failures that can significantly compromise the functioning of the network. We uncover a striking phenomenon: memory associated with nodal recovery can counter-intuitively make the network more resilient against large-scale failures. In natural systems, the intrinsic non-Markovian characteristic of nodal recovery may thus be one reason for their resilience. In engineering design, incorporating certain non-Markovian features into the network may be beneficial to equipping it with a strong resilient capability to resist catastrophic failures.

[1] State Key Laboratory of Precision Spectroscopy and School of Physics and Electronic Science, East China Normal University, Shanghai 200241, China. [2] Shanghai Key Laboratory of Multidimensional Information Processing, East China Normal University, Shanghai 200241, China. [3] School of Physical Science and Technology, Soochow University, Suzhou 215006, China. [4] Department of Physics, The Chinese University of Hong Kong, Shatin, Hong Kong SAR, China. [5] School of Electrical, Computer and Energy Engineering, Arizona State University, Tempe, AZ 85287, USA. ✉email: tangminghan007@gmail.com; zhliu@phy.ecnu.edu.cn

The dynamics of failure propagation on complex networks constitute an active area of research in network science and engineering with significant and broad applications. This is because the functioning of a modern society relies on the cooperative working of many networked systems such as the electrical power grids, various transportation networks, computer and communication networks, and business networks, but these networks typically possess a complex structure and are vulnerable to failures and intentional attacks. Among the diverse failure scenarios, one of the most severe types is cascading failures[1], where the failure of some nodes would cause their neighbors to fail and the process would propagate to the entire network, disabling a large fraction of the nodes and causing malfunctioning of the system at a large scale[2–15]. Classic examples of cascading failures includes power blackout—the collapse of power grids[5,6], traffic jams[16], and even economic depression[14,17]. Previous studies mostly focused on how cascading failures occur, how network structures and failure propagation are related, and on network robustness and vulnerability to failure propagation[18–22].

A tacit assumption employed in many previous studies of cascading failures is irreversible failure propagation, where a node, if it has failed, cannot recover and is no longer able to function actively. A failed node is then removed from the network completely, including all the links associated with it. There are real-world situations of networked systems, such as financial and transportation networks, where failed nodes can recover from malfunctioning spontaneously after a collapse[23–28]. In general, there are two types of failure-and-recovery scenarios[29]: internal and external. In the first type, a node fails because of internal causes (e.g., the occurrence of some abnormal or undesired dynamical behaviors within the node), which is independent of the states of its neighbors. In this case, the node can recover spontaneously after a period of time. An example is the failure of a company characterized by a drop in its market value due to poor management, followed by recovery due to internal restructuring. The second type is external failures, where a node's failure is externally triggered, e.g., by the failures of its neighboring nodes. After a period of time, as its local "environment" is improved, the node is able to recover spontaneously. The time of recovery depends not only on the specific type of failure-and-recovery mechanism, i.e., whether internal or external, but also on the individual node and its position in the network. For example, for a given node in the network, it may take longer to complete an internal restructuring process to recover from a failure due to an internal than an external cause. Previous computation and mean-field analysis have revealed that cascading dynamics incorporating a failure-and-recovery mechanism can exhibit a rich variety of phenomena such as phase transitions, hysteresis, and phase flipping[29–33]. With respect to the resilience responses of networks, the effects of removing a fraction of nodes and links on network functions were studied[34–37], demonstrating that resilience can be used to characterize the critical functionality of the network with applications in complex infrastructure engineering[36,37].

In spite of the variations in the recovery dynamics across networks or even nodes in the same network, generally the process can be classified into two distinct types: Markovian and non-Markovian. In a Markovian recovery process, an event occurs at a fixed rate and the interevent time follows an exponential distribution[38–40], rendering memoryless the process. On the contrary, a non-Markovian recovery (NMR) process has memory, as the current state of a node depends not only on the most recent state but also on the previous states. In this case, the interevent time distribution is not exponential but typically exhibits a heavy tail. For example, in human activity and interaction dynamics, the occurrences of contacts among the individuals in a social network can be characteristically non-Markovian, for which there is mounting empirical evidence[41–48]. Non-Markovian type of recovery process also occurs in biochemical reactions[49] and in the financial markets[12,50]. We note that, in the context of spreading dynamics on complex networks, the effects of the non-Markovian process, due to its high relevance to the real world, have attracted growing attention[51–58]. From the point of view of mathematical analysis, incorporating memories into the dynamical process makes analytic treatment challenging.

While the impacts of non-Markovian processes on spreading dynamics have been reasonably well-documented[51–58], there has been little work so far addressing the influence of non-Markovian recovery process on failure propagation dynamics. In this paper, we address this issue systematically through a comparison study of two types of dynamical processes: one with Markovian and another with NMR. In the Markovian recovery (MR) model, failures due to internal and external causes will recover with different constant rates. In the NMR model, such a constant rate cannot be defined. We thus resort to the recovery time. In particular, we assume that the failed nodes due to internal and external causes will take different time to recover, so a memory effect is naturally built into the model. For each model, we develop a mean-field theory and an analysis based on the pair approximation (PA)[29,59–62] that retains the two-node correlation but ignores any correlation of higher orders. Comparing results with numerical simulations indicates that both mean-field theory and PA analysis capture the key features of the failure propagation dynamics qualitatively, but the PA analysis yields results that are in better quantitative agreement with numerics. The counterintuitive and striking phenomenon is then that non-Markovian character with a memory effect makes the network more resilient against large-scale failures. There are two implications. Firstly, in physical, biological, or other natural networked systems, the intrinsic non-Markovian character of nodal recovery may be one reason for resilience of these networks and their existence in a harsh environment. Secondly, in engineering and infrastructure design, incorporating certain non-Markovian features into the network may help strengthen its resilience and robustness.

Results

Spontaneous recovery models. For general failure propagation dynamics on a network, a node can be in one of two states: an active (labeled as A-type) state in which the node functions properly and an inactive state (I-type) in which the node has failed. To distinguish the causes for a node to become inactive, we label an inactive node due to internal or external failure as X-type or Y-type, respectively.

In the NMR model, an A-type node may fail spontaneously at the rate β_1 to become an X-type node, or it may fail at the rate β_2 to become a Y-type node when the number of its A-type neighboring nodes is less than or equal to a threshold integer value m that sets the limit on neighboring support for proper functioning of a node. Without loss of generality, we assume that external failures occur more frequently than internal failures: $\beta_1 < \beta_2$. This is often the case as internal failures can be made less probable by building up the capability of the nodes through better equipment and/or management, while external failures are uncontrollable and more difficult to avoid. For examples, falling stocks may be the result of unanticipated changes in the market rather than poor management. In a road network, failures are caused more often by congestion than by physical failures. Once a node becomes inactive, it takes time τ_1 to recover from an internal failure (when the node is of the X-type) or time τ_2 to recover from an external failure (when the node is of the Y-type). The non-Markovian characteristic is taken into account through

the incorporation of a memory effect into the model. In particular, the nodes that will recover at time t constitute those that were turned into X-type inactive nodes at the time $t - \tau_1$ and those turned into Y-type inactive nodes at the time $t - \tau_2$. Here, we assume $\tau_1 > \tau_2$, for the reason that repairing a node or restructuring the management due to the malfunctioning of the node itself would need more time. For example, reorganizing a company or repairing a road often takes more time. The failure processes characterized by the rates β_1 and β_2 as well as the recovery processes as determined by τ_1 and τ_2 are schematically illustrated in Fig. 1.

Note that the case of $\tau_1 < \tau_2$ may also arise in the real world. For example, for an infrastructure network in civil engineering, when an earthquake strikes and destroys buildings (nodes), the time to rebuild can be longer than that required for recovering from internal failures, e.g., the collapse of a roof due to some material failure. Our computations of this case yield qualitatively similar results to those in the case of $\tau_1 > \tau_2$—see Supplementary Note 3 for detail.

The MR and NMR models differ only in the recovery processes. In the MR model, an inactive node of the X-type or the Y-type recovers at a constant rate μ_1 or μ_2, respectively, as illustrated in Fig. 1. Consequently, the number of nodes recovered at time t depends only on the number of inactive nodes of both X-type and Y-type at the previous time step.

To develop theories for failure propagation on networks with MR or NMR recovery process and to identify the key differences

between the two type of dynamics, we focus on random regular networks. In the numerical simulations, we use a relatively large network size $N = 3 \times 10^4$ with the degree $k = 35$. In the NMR model, the recovery times are taken to be $\tau_1 = 100$ and $\tau_2 = 1$ for the X-type and Y-type of nodes, respectively. In the MR model, the values of the recovery rates are set to be $\mu_1 = 1/\tau_1 = 0.01$ and $\mu_2 = 1/\tau_2 = 1$ so that they correspond to the same scales for the recovery times in the NMR model (see Supplementary Note 1 for a more detailed explanation). The threshold values in both models are $m = 15$. Synchronous updating is invoked in simulations with the time step $\Delta t = 0.01$.

Markovian recovery process. *Mean-field theory*: We start with setting up the dynamical equations for MR dynamics and comparing results with simulations. Based on the mean-field theory in "Mean-field theory for MR dynamics" of "Methods" section, we first examine the behavior of $E_t([I])$ in Eq. (4). Figure 2a shows the dependence of $E_t([I])$ on the fraction of failed nodes $[I]$. It can be seen that E_t exhibits two different types of behaviors over a large part of $[I]$: $E_t \sim 0$ for a wide range of small $[I]$ values (low failure) and $E_t \sim 1$ for a range of large $[I]$ values (high failure). In the low failure state, external failure events rarely occur. In the high failure state, an active node is supported by an insufficient number of active neighbors and external failure events almost always happen. It implies that the stationary state $[I]$ can possess two branches: setting $E_t = 0$ in Eq. (5) gives $[I] = 1 - 1/(\beta_1/\mu_1 + 1)$ as the low-failure branch, while setting $E_t = 1$ gives $[I] = 1 - 1/(\beta_2/\mu_2 + \beta_1/\mu_1 + 1)$ as the high-failure branch. The two branches are shown in Fig. 2b (dashed and solid curves) in terms of the dependence of $[I]$ on β_1, for $\mu_1 = 0.01$, $\beta_2 = 2$, and $\mu_2 = 1$ as an example. To check which branch the system would take on and whether there are two states for some range of parameters, the simulation results for moving the value of β_1 up (circles) and down (squares) are shown in Fig. 2b for comparison. As the values of β_1 are increased or decreased, the initial state is taken to be the final state corresponding to the previous value of β_1—the adiabatic process. The results indicate that: (i) the values of $[I]$ from simulations follow the two branches given by the mean-field approximation, and (ii) the low-failure (high-failure) branch is followed when moving β_1 up (down) until a particular value at which there is a jump to the high-failure (low-failure) branch—the signature of a hysteresis. The results also imply that if one starts from the initial conditions $[X]_0 \neq 0$ and $[Y]_0 = 0$, there exists a critical value of $\beta_c \approx 0.007$ for a sudden increase in the number of failed nodes when $[X]_0$ is small as the system will

A $\xrightarrow{\beta_1}$ X $\xrightarrow{\tau_1 \, (\mu_1)}$ A

A $\xrightarrow[if \; n \leq m]{\beta_2}$ Y $\xrightarrow{\tau_2 \, (\mu_2)}$ A
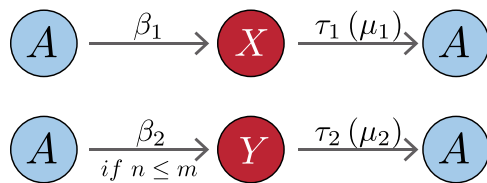
Fig. 1 Schematic illustration of NMR and MR models. An active (A-type) node may fail spontaneously at the rate β_1 to become an X-type node due to internal causes, or it may fail at the rate β_2 to become a Y-type node when the number of its A-type neighbors n is less than or equal to a threshold m setting the necessary neighboring support for the proper functioning of a node. In the NMR model, the X-type and Y-type nodes take the time duration τ_1 and τ_2 from the time they are generated to recover, respectively. In the MR model, the X-type and Y-type nodes recover, respectively at the rates μ_1 and μ_2.
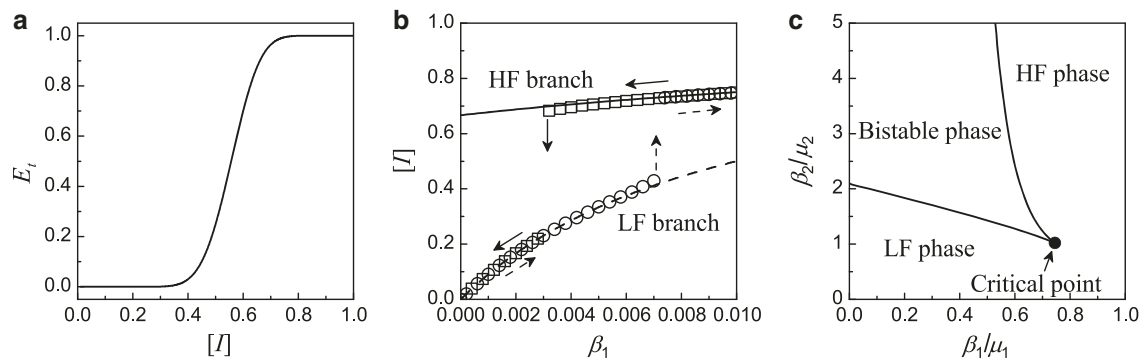
Fig. 2 Behaviors of MR model. a Probability $E_t([I])$ in the mean-field theory [Eq. (4)] as a function of $[I]$. **b** Dependence of $[I]$ on β_1 in the steady state for $\beta_2 = 2.0$, $\mu_1 = 0.01$, and $\mu_2 = 1$. The high-failure (solid curve) and low-failure (dashed curve) branches are calculated by the mean-field theory. The simulation data are obtained by swabbing β_1 up and down in step of 0.002, starting with $[I]_0 = 0$ for $\beta_1 = 0$. The final state of a value of β_1 is used as the initial state of the simulations for the next value of β_1. The arrows indicate the simulation results when the value of β_1 moves up and down. **c** Phase diagram on the β_2/μ_2-β_1/μ_1 plane as predicted by the mean-field theory. Systems in the bistable phase will evolve either to a high-failure or a low-failure phase depending on the initial conditions. Beyond the critical point, there is no distinction between the low-failure and high-failure phases.
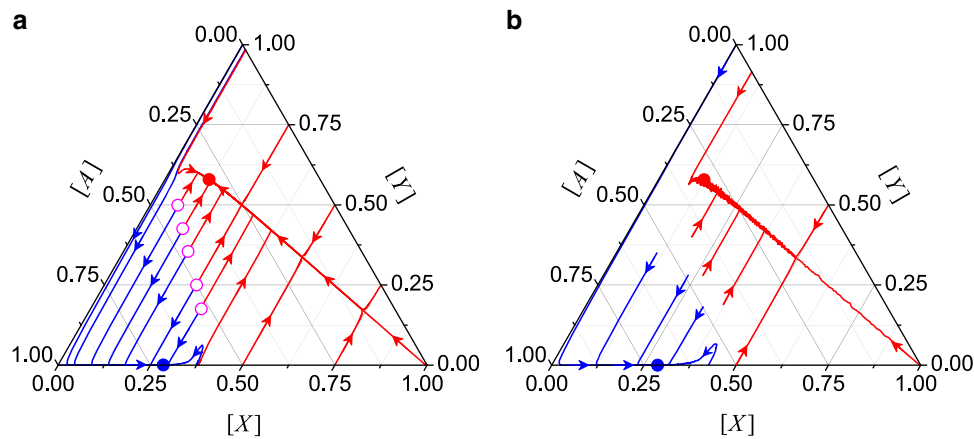
Fig. 3 Evolutionary properties of MR dynamics. The dynamical process can be represented as a flow diagram with the lines showing how the fractions of $[X]$, $[Y]$, and $[A]$ evolve in time. The solid circles are the fixed points that the system will finally evolve into. **a** Theoretical calculations based on the mean-field theory. The open circles trace out a separatrix, with systems on different sides evolving into different fixed points. **b** Simulation results. The system parameters are $\beta_1 = 0.004$, $\beta_2 = 2.0$, $\mu_1 = 0.01$, and $\mu_2 = 1$.

follow the low-failure branch. However, for large $[X]_0$, the critical value β_c becomes $\beta_c \approx 0.003$ as the system will follow the high-failure branch. A plot of β_c against $[X]_0$ will therefore exhibit two plateaus with $\beta_c \approx 0.007$ for small $[X]_0$ and $\beta_c \approx 0.003$ for large $[X]_0$.

The mean-field approximation not only simplifies the analysis but also provides insights into the dynamical process. For example, the mean-field theory suggests the ratios β_1/μ_1 and β_2/μ_2 as key parameters. In general, solutions can be obtained numerically by solving Eq. (5) together with Eq. (4). The results are shown in Fig. 2c as a phase diagram. For parameters falling into the regions corresponding to the low-failure (high-failure) phase, the system will evolve into a low-failure (high-failure) state. For parameters in the bistable phase, the system will evolve either to a low-failure or a high-failure state, depending on the initial conditions. The high-failure and low-failure phase boundaries meet at the critical point determined by $\beta_1/\mu_1 \approx 0.745$ and $\beta_2/\mu_2 \approx 1.020$.

In addition to the stationary state, the evolution of the system can also be studied by iterating Eqs. (1) and (2) for a given initial condition. Figure 3a shows the evolution of the MR dynamics as obtained by the mean-field theory for $\beta_1 = 0.004$ and $\beta_2 = 2$. In the three-dimensional space formed by $[A]$, $[X]$, and $[Y]$, the sum rule $[A] + [X] + [Y] = 1$ defines a triangular plane, as shown in Fig. 3. At any time t, the state of the system is characterized by a point in the plane. The results show that the MR dynamics will evolve into either the low-failure or the high-failure state (filled circles), depending on where the system begins. The mean-field theory also gives a separatrix, the line traced out by the open circles, where the system will evolve into a different state starting from a point on a different side of the separatrix. For $[X]_0 > 0.38$, the system will evolve to a high-failure state with ($[X]$, $[Y]$, $[A]$) given approximately by (0.119, 0.580, 0.301). For $[X]_0 < 0.38$, the system may evolve to the high-failure state or a low-failure state at around (0.285, 0, 0.715). Numerical results are shown in Fig. 3b, verifying all the features predicted by the mean-field theory. For example, the high-failure state is given by ($[X]$, $[Y]$, $[A]$) ~ (0.124, 0.579, 0.298) and the low-failure state at around (0.287, 0, 0.713), both are quite close to the values predicted by the mean-field theory.

Pairwise approximation theory for the MR model: It is possible to formulate a theory that takes into account of two-node spatial correlation based on the pairwise approximation (PA). The basic idea is to follow the evolution of different types of links, i.e., links

that connect different pairs of neighboring nodes[62]. The PA method has been used widely in studying epidemic and information spreading[63–65], and in coevolving voter models and adaptive games with two or more strategies[66–69]. In "Effect of nodal correlation: pairwise approximation for the MR model" of "Methods" section, we develop a PA based theory for the MR model.

Figure 4 presents a comparison of the predictions of the PA analysis and mean-field theory with the numerical results, where Fig. 4a shows the time evolution of $[X]_t$ and $[Y]_t$ from the initial state $[X]_0 = [Y]_0 = 0$ for $\beta_1 = 0.009$, $\beta_2 = 2.0$, $\mu_1 = 0.01$, and $\mu_2 = 1$. While both mean-field and PA theories capture the key features in time evolution, the results of PA are in better agreement with those from simulations. It is useful to understand the dynamical behaviors in the MR model qualitatively (so as to enable a meaningful comparison with those of the NMR model later). For this purpose, we identify several stages in the time evolution as marked in Fig. 4a. In the early stage, i.e., $t \in [t_O, t_A]$, most nodes are active and they have more active neighbors, violating the condition $n_A \leq m$. As a result, only internal failures occur and $[X]_t$ grows but $[Y]_t$ decreases and eventually vanishes. For $t \in [t_A, t_B]$, $[X]_t$, active nodes start to fail into Y-type nodes, leading to fewer active nodes in the system and triggering more external nodal failures. This results in the observed rapid increase in $[Y]$. In the later stage $t \in [t_B, t_C]$, there are more failed nodes than active ones. While the failed nodes of X and Y types can recover with their respective rates, the remaining or recovered active nodes will more likely fail again through external than internal causes due to the many failed nodes surrounding the active nodes. Consequently, in this later stage, $[Y]_t$ increases and $[X]_t$ decreases toward their respective steady-state values for $t \to \infty$, with $[Y] > [X]$ when the system evolves into a high-failure state. The PA analysis captures the behavior of $[X]_t$ over time and the onset of $[Y]_t$ better than the mean-field analysis. Figure 4b shows the phase diagram for $\mu_1 = 0.01$ and $\mu_2 = 1.0$. The mean-field phase diagram is the same as that shown in Fig. 2c, where it can be seen that the results of the PA analysis (solid curves) are indeed in better agreement with the simulation results than the predictions of the single-node mean-field theory.

Note that Fig. 2 reveals the emergence of a critical value of β_c in the spontaneous failure rate beyond which the system incurs a large-scale failure starting from the initial conditions $[X]_0 \neq 0$ and $[Y]_0 = 0$. The critical rate β_c is calculated by starting the system from the initial conditions for different values of β_1 (for a fixed
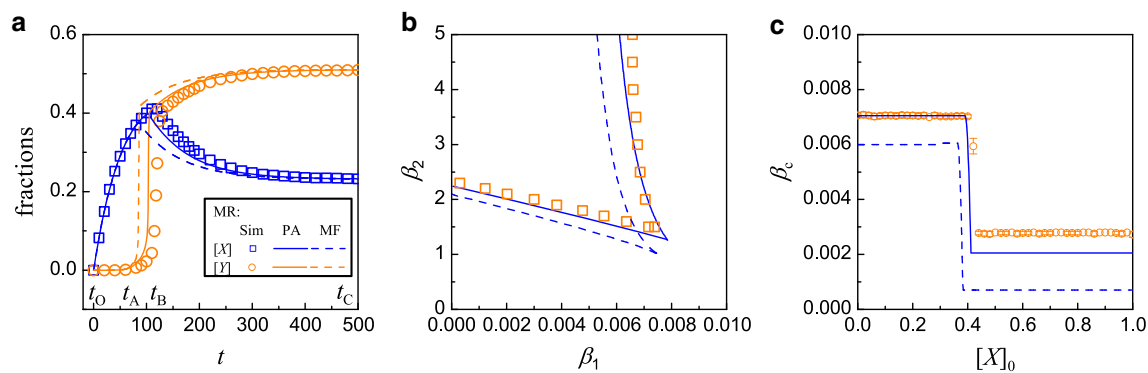
Fig. 4 Comparison of simulation results with predictions from PA analysis and mean-field theory for the MR model. a Time evolution of the fraction of inactive nodes. The initial conditions are $[X]_0 = [Y]_0 = 0$. The parameter values are $\beta_1 = 0.009$, $\beta_2 = 2.0$, $\mu_1 = 0.01$, and $\mu_2 = 1.0$. Several time instants are marked to facilitate visualization of the time evolution in different stages: $t_O = 0$, $t_A = 60$, $t_B = 120.7$, and $t_C = 480$. **b** Phase diagram on the $(\beta_2 - \beta_1)$ parameter plane. Other parameters are $\mu_1 = 0.01$, and $\mu_2 = 1.0$. **c** Dependence of β_c on the initial value of $[X]_0$, with $[Y]_0 = 0$. The solid (dashed) curve is calculated by the PA (mean-field) theory, and the symbols are for simulation results obtained by averaging over 100 realizations.

value of $\beta_2 = 2.0$) and search for the value of β_1 beyond which the system attains a high-failure state (see Supplementary Fig. 1 in Supplementary Note 2). The critical value thus depends on $[X]_0$, the initial fraction of failed nodes due to an internal mechanism. Figure 4c shows the numerically obtained functional relation $\beta_c([X]_0)$ (open circles), together with two types of theoretical prediction (PA analysis and mean-field theory). As the initial fraction $[X]_0$ is increased from a near zero value, β_c maintains at a relatively higher constant value (about 0.007). As $[X]_0$ increases through the value of about 0.4, the value of the critical rate suddenly decreases to about 0.003. We see that, again, the prediction of the abrupt change in β_c by the PA analysis is more accurate than that by the mean-field theory.

What is the physical meaning of the abrupt decrease in the critical value of the spontaneous failure rate as displayed in Fig. 4c? A higher value of β_c means that the network system is more resilient to large-scale failures as it requires a larger rate value to drive the system into a high-failure state. As the fraction of initially failed nodes is increased, the network as a whole is more prone to large-scale failure so we expect the value of β_c to decrease. Because of the lack of any memory effect in the ideal, Markovian type of recovery process, i.e., after a node fails, it either recovers instantaneously or does not recover (with probabilities determined by the rate of recovery), we expect a characteristic change in the system dynamics as characterized by the value of the critical rate β_c to occur in an abrupt manner. Indeed, as Fig. 4c reveals, as the fraction of initially failed nodes is increased through a threshold value, there is a sudden decrease of about 50% in the value of β_c, giving rise to a first-order type of transition. This behavior of abrupt transition may not occur in reality because of the assumed Markovian recovery process, which is ideal and cannot be expected to arise typically in the physical world. In the next section, we will demonstrate that making the dynamics more physical by assuming non-Markovian type of recovery process will drastically alter the picture of transition in Fig. 4c.

Non-Markovian recovery process. To analyze failure propagation dynamics in systems with NMR, a viable approach is to construct difference equations that relate the fractions of types of nodes and links at time $t + \Delta t$ to those at time t. It is necessary to keep track of the time when a node becomes the X or Y type as well as the time at which a link becomes type UV. In "Pairwise approximation theory for the NMR model" of "Methods" section, we develop a PA analysis for the NMR model. Figure 5 shows the simulation results from the NMR model, together with the

predictions of the PA analysis and mean-field approximation for $\Delta t = 0.01$. The time evolution of $[X]_t$ and $[Y]_t$ is shown for the parameter setting $\beta_1 = 0.009$, $\beta_2 = 2.0$, $\tau_1 = 100$ (thus $\mu_1 = 0.01$), and $\tau_2 = 1$ (thus $\mu_2 = 1$). The initial conditions are $[X]_0 = [Y]_0 = 0$. Both theories capture the key features of the dynamics. Comparing with results from the MR model [e.g., Fig. 4a], we see that the time evolution of the dynamical variables in the NMR model is different from that in the MR model, in spite of the approximately identical steady-state values.

To describe the key features of the NMR model, we divide the evolution into five stages with the respective time intervals $[t_O, t_A]$, $[t_A, t_B]$, $[t_B, t_C]$, $[t_C, t_D]$, and $[t_D, t_E]$, as shown in Fig. 5a. In the earliest stage $[t_O, t_A]$, $[X]_t$ increases due to internal failures but $[X]_t$ is insufficient to cause external failures. The behavior is similar to that in the MR model, but the duration is shorter and the rise in $[X]_t$ is steeper in the NMR model. The reason is that the memory effect in NMR model allows the recovery of X-type nodes to take place only after τ_1 steps, while the recovery occurs probabilistically in the MR model. In the narrow time window of $[t_A, t_B]$, $[X]_t$ attains a level high enough to trigger the onset of many external failures. As a result, the failed nodes constitute the majority in the system and $[A]_t$ decreases sharply, giving rise to the sharp increase in $[Y]_t$. The Y-type nodes recover deterministically after τ_2 ($\tau_2 < \tau_1$) into active nodes. In the period $[t_B, t_C]$, the recovery of Y-type nodes refuels the system with active nodes that can participate in two paths: more internal and external failures. For $t_C < \tau_1$, the existing X-type nodes have yet to recover and $[X]_t$ continues to increase but at a slower pace due to the external failure path, while $[A]_t$ reduces slightly.

In the time window $[t_C, t_D]$, the initial internally failed nodes begin to recover as $t_C > \tau_1$, in addition to the recovery of the Y-type nodes. The A-type nodes due to recovery will be more likely to become Y-type as the failed nodes remain the majority (due to the parameter setting $\beta_2 > \beta_1$ in this example). This leads to the observed increase in $[Y]_t$ and decrease in $[X]_t$ in the time interval $[t_C, t_D]$. In the final stage $[t_D, t_E]$, $[X]_t$ stops decreasing because the recovery of X-type nodes at the time $t \gtrsim t_D$ is due to those failed internally at $t \gtrsim t_B$ for which the number was small. However, the recovery of Y-type nodes at a shorter time scale supplies fresh active nodes. The fraction of failed nodes $[X]_t + [Y]_t$ is so high, i.e., approaching the high-failure state, that the dynamics lead to a higher steady value of $[Y]$ than $[X]$ in long time. For time well beyond t_D, both $[X]$ and $[Y]$ become steady.

Figure 5b shows the phase diagram of the NMR model analogous to Fig. 4b for the MR model, with $\mu_1 = 0.01$ and $\mu_2 = 1.0$. The results of the PA analysis (solid curve) are in better
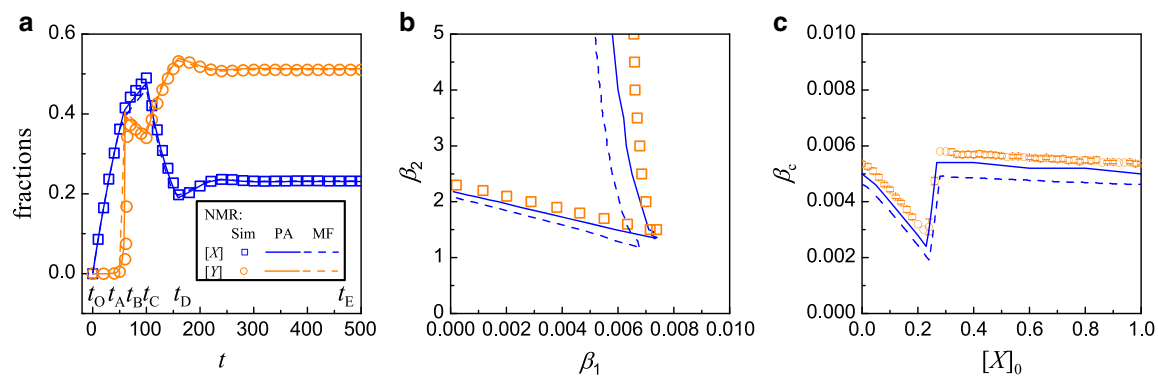
Fig. 5 Benefit of non-Markovian recovery to making the network more resilient against large-scale failures. Shown are results from the NMR model through simulations, PA analysis, and mean-field theory. **a** Time evolution of inactive nodes from the initial conditions $[X]_0 = [Y]_0 = 0$, for $\beta_1 = 0.009$, $\beta_2 = 2.0$, $\tau_1 = 100$ (thus $\mu_1 = 0.01$), and $\tau_2 = 1.0$ (thus $\mu_2 = 1.0$). A number of time instants are marked for better visualization of the time evolution in different stages: $t_O = 0$, $t_A = 43.51$, $t_B = 64.68$, $t_C = 100$, $t_D = 164.51$, and $t_E = 480$. **b** Phase diagram in the ($\beta_2 - \beta_1$) parameter plane for $\tau_1 = 100$ and $\tau_2 = 1.0$. The symbols are numerical results, and the solid and dashed curves are obtained from the PA analysis and mean-field theory, respectively. **c** Dependence of β_c for reaching a high-failure state on the initial value of $[X]_0$ with $[Y]_0 = 0$. The error bars with the simulation results are about 6×10^{-5}, which are obtained by averaging over 100 realizations.

agreement with the simulation results than those obtained from the mean-field theory (dashed curve). The difference in dynamics in the NMR model also alters the dependence of β_c to sustain a high-failure state on $[X]_0$. Carrying out the same analysis as for the MR model (see Supplementary Fig. 1 in Supplementary Note 2 for details), we get the relationship $\beta_c([X]_0)$ for attaining a high-failure state for a given initial condition, as shown in Fig. 5c. The pair approximation, again, gives more accurate prediction than that from the mean-field theory.

The result in Fig. 5c demonstrates the striking effect of non-Markovian type of recovery with memory on the failure propagation dynamics, which is in stark contrast to the ideal case of Markovian process as exemplified in Fig. 4c. In particular, as the fraction $[X]_0$ of initially failed nodes is increased from a near zero value to one, the value of β_c begins to decrease continuously and smoothly until it reaches a minimum, at which β_c increases relatively more rapidly to a high value of about 0.006 for $[X]_0 \approx 0.3$. For $[X]_0 > 0.3$, the value of β_c remains approximately constant at 0.006. Comparing Fig. 5c with Fig. 4c, we see two major, characteristic differences. Firstly, the behavior of an abrupt decrease in the Markovian case is replaced by a gradual process in the non-Markovian case, essentially converting a first-order like process to a second-order one. Secondly and more importantly, β_c recovers from its minimum value and maintains at a high value regardless of the value of $[X]_0$ insofar as it exceeds about 30%. This means that, the system can maintain its degree of resilience even when the initial fraction of failed nodes reaches 100%! This contrasts squarely the behavior in the Markovian case, where the system resilience is reduced dramatically even when only about 40% of the nodes failed initially. In this sense, we say that a non-Markovian type of memory effect makes the network system more resilient against failure propagation.

While the behavior in Fig. 5c is counterintuitive, a heuristic reason is as follows. For an initial state with many initial X-type nodes, the few remaining nodes will switch from being active to the Y-type and back. All the initial X-type nodes will have to wait for the time period τ_1 to recover. At that time, the system becomes one with only a few failed nodes—effectively equivalent to one with small $[X]_0$ value and requiring a larger β_c value to evolve into the high-failure state. In a range of small $[X]_0$, a smaller β_c can already cause more active nodes to become Y-type, helping maintain the system in a high-failure state as described

for Fig. 5a. Theoretical support for the behavior is provided by the PA analysis and mean-field theory, as shown in Fig. 5c.

In addition to the different time evolution in the MR and NMR models, there are also cases where the same initial conditions $[X]_0$, $[Y]_0$, and $[A]_0$ would lead to different final states. Figure 6 shows the final states starting from any $[X]_0$ and $[Y]_0$ in the $[X]_0 - [Y]_0$ plane (the basin structure), with $\beta_1 = 0.004$, $\beta_2 = 2.0$, $\mu_1 = 0.01$, and $\mu_2 = 1.0$. The results from the mean-field theory (Fig. 6a) and direct simulations (Fig. 6b) show essentially the same features. (Results from the initial-condition setting $[X]_0 \neq 0$ and $[Y]_0 = 0.0$ are presented in Supplementary Fig. 2 of Supplementary Note 2.) It is useful to contrast the final states of the MR and NMR models. From Fig. 3, an initial state, e.g., $[X]_0 = [Y]_0 = 0.5$, will evolve into a high-failure state in the MR model, but it will end up in a low-failure state in the NMR model. This means that, the NMR process can make the system more resilient to failures. (More examples can be found in Supplementary Fig. 3 of Supplementary Note 2 where different steady states from the two models are presented.)

MR and NMR dynamics on heterogeneous networks. So far our analysis and simulations have been carried out for MR and NMR dynamics on random regular networks. We find that altering the network structure causes little change in the qualitative results. For example, we have carried out simulations on scale-free networks of size $N = 3 \times 10^4$ with degree range $[k_{min}, \sqrt{N}]$ and degree distribution $P(k) \sim k^{-\gamma}$. Figure 7 shows the results of β_c versus $[X]_0$ for the MR and NMR dynamics for networks with $\gamma = 3$. Because of the heterogeneity in the nodal degree distribution, the threshold on external failure is given in terms of the fraction one-half of the failed neighbors.

Comparing results with Fig. 4c for MR dynamics and Fig. 5c for NMR dynamics in random regular networks, we see that the key features are similar when the underlying random regular networks are replaced by scale-free networks. We have also carried out numerical simulations on four additional types of synthetic and empirical networks: (a) networks with degree–degree correlation, (b) networks with a community structure, (c) empirical arenas-email network, and (d) empirical friendship-hamster network, with results presented in Supplementary Notes 4 and 5 for the former and latter two cases, respectively. These results, together with Fig. 7, suggest that, for
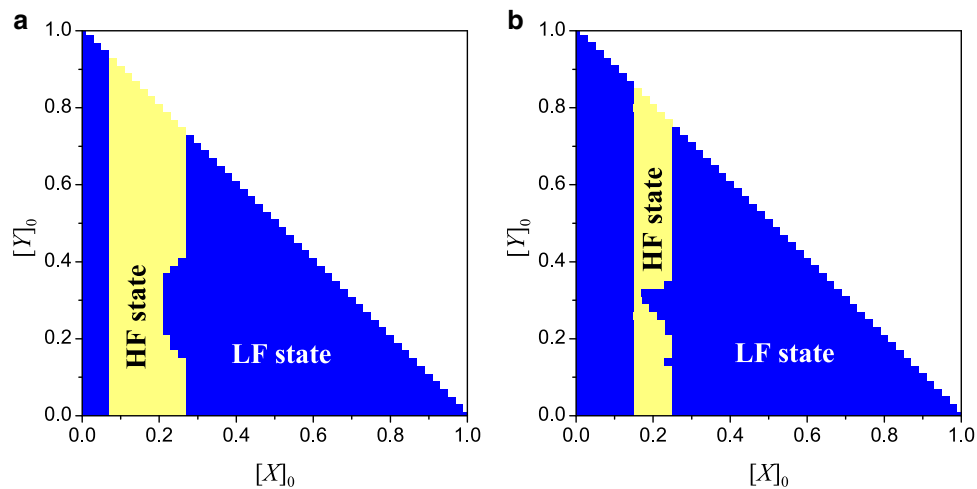
Fig. 6 Basin structure of NMR model. On the $[X]_0 - [Y]_0$ plane, basin structure from **a** mean-field theory and **b** simulations. The colors indicate the nature of the steady states given the initial conditions ($[X]_0, [Y]_0$). The parameter setting is the same as that in Fig. 3 for the MR model. The simulation results are obtained by averaging over ten statistical realizations.
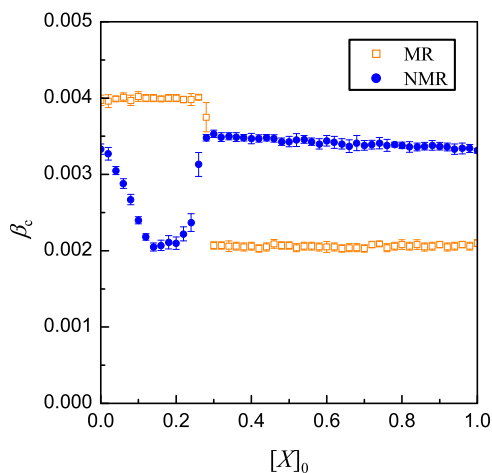
Fig. 7 MR and NMR dynamics on heterogeneous networks. The networks are scale-free with $N = 30,000$ nodes, degree exponent $\gamma = 3$, $k_{min} = 6$ and $k_{max} = 173$. Shown is the dependence of β_c for reaching a high-failure state on the initial value of $[X]_0$, with $[Y]_0 = 0$, in the MR and NMR models for $\beta_2 = 1.9$, $\mu_1 = 0.01$, $\mu_2 = 1$, $\tau_1 = 100$, and $\tau_2 = 1$. The results qualitatively consistent with those in Fig. 4c for MR dynamics and in Fig. 5c for NMR dynamics on random regular networks.

heterogeneous networks, a non-Markovian process tends to enhance the network resilience against large-scale failures.

Discussion

The intrinsic memory effect associated with non-Markovian processes makes it challenging to analyze the underlying network dynamics, new and surprising phenomena can arise. Most previous studies treated Markovian processes through either a mean-field type of theory[60,61] or an effective degree approach[59]. For non-Markovian processes, the mean-field approximation can still be applied[29,31–33], but it is necessary to invoke a higher-order theory such as the PA analysis. Our work presents such an example in the context of failure propagation in complex networks.

Our study has demonstrated that, in both models, the network can evolve into a low-failure or a high-failure state, with the latter corresponding to the undesired state of large-scale failure. Both the mean-field and PA theories are capable of predicting the

dynamical behaviors of failure propagation, and the performances of the theories are gauged by simulation results, revealing that the more laborious pair approximation gives results in better quantitative agreement with the numerics. Our systematic computations on different complex networks and two types of theoretical analyses have uncovered a striking phenomenon: the non-Markovian memory effect in the nodal recovery can counterintuitively make the network more resilient against large-scale failures.

Our finding also calls for the incorporation of non-Markovian type of memory factors into the design of communication, computer, and infrastructure networks in various engineering disciplines. We hope our work will stimulate interest in examining and exploiting non-Markovian processes in various network dynamical processes. We have carried out a systematic study of the effects of Markovian versus non-Markovian recovery on network synchronization using the paradigmatic Kuramoto network model, with the main finding that non-Markovian recovery makes the network more resilient against large-scale breakdown of synchronization (Supplementary Note 6).

Methods

Mean-field theory for MR dynamics. Let $[A]_t$, $[X]_t$, and $[Y]_t$ be the fractions of A-type, X-type, and Y-type nodes in the system at time t, respectively. A hierarchical set of dynamical equations for the MR model can be constructed to include increasingly longer spatial correlation. The equations for the evolution of the fractions of different types of nodes are:

$$\frac{\mathrm{d}[X]_t}{\mathrm{d}t} = \beta_1 [A]_t - \mu_1 [X]_t, \tag{1}$$

and

$$\frac{\mathrm{d}[Y]_t}{\mathrm{d}t} = \beta_2 E_t [A]_t - \mu_2 [Y]_t, \tag{2}$$

where the first term in each equation gives the supply to $[X]$ ($[Y]$) due to internal (external) failures and the second term represents the drop in $[X]$ ($[Y]$) due to recovery. Note that, because of the relation

$$[A]_t = 1 - [X]_t - [Y]_t \equiv 1 - [I]_t, \tag{3}$$

an equation for $[A]_t$ is unnecessary. The quantity E_t is the probability of an A-type node having $j \leq m$ neighbors of A-type nodes at time t and thus the node will be infected at the rate β_2.

In general, the quantity E_t involves the correlation between two neighboring nodes. To connect Eqs. (1) and (2) so as to retain the simplicity of a single-node theory, we use the approximation

$$E_t([I]) = \sum_{j=0}^{m} C_k^{k-j} ([I]_t)^{k-j} (1 - [I]_t)^j, \tag{4}$$
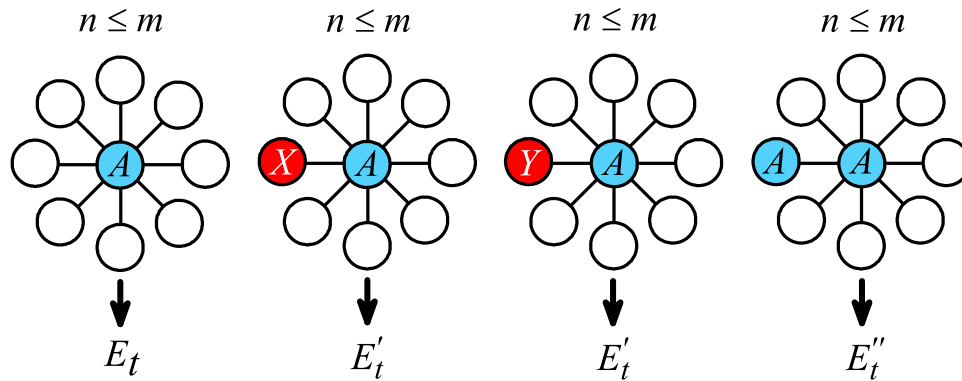
Fig. 8 Schematic diagram for the PA analysis of the MR model. The quantities are E_t, E'_t and E''_t. The blue (red) color indicates a node in the active (failure) state. Open circles are nodes that may take on A, X, or Y state. In the PA equations, E_t is the probability of an A-type node having $n \leq m$ neighbors of A-type nodes at time t, E'_t is the probability of an A-type node having $n \leq m$ A-type neighbors among its $(k-1)$ neighbors given that one neighbor is inactive, and E''_t is the probability of an A-type node having $n \leq m - 1$ A-type neighbors among its $(k-1)$ neighbors given that one neighbor is active.

where $C_k^{k-j} = k!/(j!(k-j)!)$. Equations (1)–(4) form a set of equations, from which the fractions of different types of nodes can be solved. This is the simplest single-site mean-field approximation for the MR dynamics that ignores any spatial correlation. Despite its simplicity, it is capable of revealing the key features in the stationary state, in which Eqs. (1) and (2) require the fraction of failed nodes $[I]$ to satisfy

$$[I] = 1 - \frac{1}{(\beta_2/\mu_2)E_t([I]) + (\beta_1/\mu_1) + 1}, \quad (5)$$

which can be solved for $[I]$ self-consistently with Eq. (4). Equation (5) implies that $[I]$ depends only on the ratios β_1/μ_1 and β_2/μ_2 within the mean-field approximation, and so are the other fractions $[A]$, $[X]$, and $[Y]$.

Effect of nodal correlation: pairwise approximation for the MR model. Our PA based analysis begins by defining $[UV]_t$ as the fractions of UV type of links in the system at time t, where $U, V \in \{A, X, Y\}$. A connection that stems out from a node can be classified by a type. For example, for a node with the current state being A-type, each link that it carries can be classified into the AA, AX, or AY type, depending on the state of the node at the other end of the link. Taking into account every link from every node, we have that the fractions of links satisfy

$$\sum_{U,V \in \{A,X,Y\}} [UV]_t = 1, \quad (6)$$

with $[UV]_t = [VU]_t$ for $U \neq V$.

In general, the equations of single-node quantities, e.g., Eq. (2), necessarily involve quantities of more extensive spatial correlation because the interplay between the failure of a node and the states of its neighboring nodes. Since $[AI]_t/[A]_t = ([AX]_t + [AY]_t)/[A]_t$ is the probability of an A-type node having an inactive node regardless of the types of the neighbors, the probability that there are exactly j neighbors of A-type and $(k-j)$ inactive neighbors of either X or Y type is

$$C_k^{k-j} \left(\frac{[AI]_t}{[A]_t}\right)^{k-j} \left(1 - \frac{[AI]_t}{[A]_t}\right)^j, \quad (7)$$

where k is the degree of the node. The quantity E_t in Eq. (2), as schematically depicted in Fig. 8a, is thus given by

$$E_t = \sum_{j=0}^{m} C_k^{k-j} \left(\frac{[AI]_t}{[A]_t}\right)^{k-j} \left(1 - \frac{[AI]_t}{[A]_t}\right)^j, \quad (8)$$

which indicates explicitly that the dynamics of single-node quantities are governed by the two-node quantity $[AI]_t$. This is reminiscence of the BBGKY (Bogoliubov-Born-Green-Kirkwood-Yvon) hierarchy of equations for the distribution functions in a system consisting of a large number of interacting particles in statistical physics[70]. Only under the approximation $[AI]_t \approx [A]_t[I]_t$ (so that the two-node correlation can be neglected) will the resulting equation be Eq. (4)—a set of single-node mean-field equations.

To proceed, we derive the dynamical equations for $[UV]_t$ that will in general involve more extensive spatial correlation. For example, a link of the type AA would evolve into a different type depending on the neighborhoods of the two nodes, effectively a small cluster of nodes. To develop a manageable approximation, we retain the two-node correlation and decouple any longer spatial correlation in terms of one-node and two-node functions. This is the idea behind PA for obtaining a closed set of equations. In particular, the dynamical equations for $[AX]_t$

and $[AA]_t$ are

$$\frac{d[AX]_t}{dt} = \mu_1[XX]_t + \mu_2[YX]_t + \beta_1[AA]_t,$$
$$- \mu_1[AX] - (\beta_1 + \beta_2 E'_t)[AX]_t, \quad (9)$$

and

$$\frac{d[AA]_t}{dt} = 2\mu_1[AX]_t + 2\mu_2[AY]_t,$$
$$- 2(\beta_1 + \beta_2 E''_t)[AA]_t, \quad (10)$$

where

$$E'_t = \sum_{j=0}^{m} C_{k-1}^{k-1-j} \left(\frac{[AI]_t}{[A]_t}\right)^{k-1-j} \left(1 - \frac{[AI]_t}{[A]_t}\right)^j, \quad (11)$$

is the probability of an A-type node having $j \leq m$ A-type neighbors among its $(k-1)$ neighbors, given that one neighbor is inactive, and

$$E''_t = \sum_{j=0}^{m-1} C_{k-1}^{k-1-j} \left(\frac{[AI]_t}{[A]_t}\right)^{k-1-j} \left(1 - \frac{[AI]_t}{[A]_t}\right)^j, \quad (12)$$

is the probability of an A-type node having $j \leq m - 1$ A-type neighbors among its $(k-1)$ neighbors, given that one neighbor is active. Figure 8 illustrates the meanings of E_t, E'_t, and E''_t schematically. The terms in Eqs. (9) and (10) account for how the recovery and failure processes affect the fractions of AX-type and AA-type links. The complete set of dynamical equations is listed in Supplementary Note 1, which can be solved iteratively to yield the temporal variations on the type of nodes and the type of links given an initial condition. The steady-state quantities can be obtained through a sufficiently large number of iterations.

Pairwise approximation theory for the NMR model. Specifically, we let $[U^l]_t$ be the fraction of nodes of type U at time t, which became type U from some other type only l time steps ago, and $[U^{l_1}V^{l_2}]_t$ be the fraction of links of the UV type when the corresponding node(s) associated with a link became that of the labeled type l_1 and l_2 time steps ago. The time evolution of the fraction of X-type nodes in the NMR model is given by

$$[X^l]_{t+\Delta t} = \{\beta_1 \Delta t[A]_t, l \in [0, \Delta t); [X^{l-\Delta t}]_t, l \in [\Delta t, \tau_1]; 0, l \in (\tau_1, \infty).. \quad (13)$$

The first line in Eq. (13) gives the new supply due to internal failure of A-type nodes in the time duration $[t, t + \Delta t)$. The second line accounts for the nodes which were inactive for a duration $l - \Delta t$ at time t but have not reached the time for recovery at time $t + \Delta t$. The third line states that all X-type nodes that came to existence τ_1 earlier have been recovered. Similarly, the time evolution of the fraction of Y-type nodes is given by

$$[Y^l]_{t+\Delta t} = \{\beta_2 \Delta t E_t[A]_t, l \in [0, \Delta t); [Y^{l-\Delta t}]_t, l \in [\Delta t, \tau_2]; 0, l \in (\tau_2, \infty),. \quad (14)$$

where E_t is defined in Eq. (8) and $[AI]_t = [AX]_t + [AY]_t$. The fractions of X-type and Y-type nodes, regardless of how long they have been in the corresponding state, are given by $[X]_t = \sum_{l=0}^{\tau_1} [X^l]_t$ and $[Y]_t = \sum_{l=0}^{\tau_2} [Y^l]_t$, respectively. The fraction of active nodes follows from $[A]_t = 1 - [X]_t - [Y]_t$.

To develop a PA analysis for failure propagation dynamics with NMR, we construct the equations for the time evolution of UV-types of links and retain

spatial correlation up to two neighboring nodes. Our derivation of the counterparts of Eqs. (13) and (14) in the MR case suggests the necessity to examine the history of the inactive nodes(s) associated with a link. For example, the time evolution of the links in $[AX^l]_t$ is governed by

$$[AX^l]_{t+\Delta t} = \begin{cases} \beta_1 \Delta t [AA]_t + \beta_1 \Delta t ([X^{\tau_1} A]_t + [Y^{\tau_2} A]_t), \\ \qquad l \in [0, \Delta t); \\ [X^{\tau_1} X^{l-\Delta t}]_t + [Y^{\tau_2} X^{l-\Delta t}]_t \\ \qquad + (1 - \beta_1 \Delta t - \beta_2 \Delta t E'_t) \\ \qquad \times [AX^{l-\Delta t}]_t, \quad l \in [\Delta t, \tau_1]; \\ 0, l \in (\tau_1, \infty), \end{cases} \quad (15)$$

where E' is defined in Eq. (11). The first line represents the new supply to AX-type of links due to an internal failure in one of the active nodes associated with a link of the AA-type, and an internal failure together with a recovery of an inactive node in a link of the XA-types and YA-types. The second line includes the supply to AX^l-type links due to recoveries from XX and YX types as well as the links of $AX^{l-\Delta t}$ type that became AX^l type in the recent duration Δt. The last line comes from the fact that an X-type node must recover after a time τ_1 since it became inactive. The fraction of links of AX-type, regardless of how long the node in the link has taken in the X-type, is given by $[AX]_t = \sum_{l=0}^{\tau_1} [AX^l]_t$. We thus have that the fraction of AA-type of links evolves in time as

$$[AA]_{t+\Delta t} = 2(1 - \beta_1 \Delta t - \beta_2 \Delta t E'_t)([AX^{\tau_1}]_t + [AY^{\tau_2}]_t),$$

$$+ [X^{\tau_1} X^{\tau_1}]_t + [Y^{\tau_2} Y^{\tau_2}]_t + 2[X^{\tau_1} Y^{\tau_2}]_t$$

$$+ (1 - 2\beta_1 \Delta t - 2\beta_2 \Delta t E''_t)[AA]_t, \quad (16)$$

where E''_t is defined in Eq. (12). Equations for other types of links can also be constructed (Supplementary Note 1). Equations (15) and (16) are analogous to Eqs. (9) and (10) in the MR model. The number of equations is determined by the divisions of τ_1 and τ_2 into the small time steps Δt, which increases rapidly when Δt is small compared with the other time scales in the NMR dynamics.

A crude approximation analogous to the mean-field theory can be developed for the NMR model by retaining only the fractions of nodes in the equations, which can be done by decoupling the two-node quantities such as $[AI]_t$ by $[AI]_t \approx [A]_t [I]_t$. The resulting equations governing the fractions of different types of nodes become

$$[X]_{t+\Delta t} = \beta_1 \Delta t [A]_t + [X]_t - [X^{\tau_1}]_t, \quad (17)$$

and

$$[Y]_{t+\Delta t} = \beta_2 \Delta t E_t [A]_t + [Y]_t - [Y^{\tau_2}]_t, \quad (18)$$

where E_t takes on the approximate form in Eq. (4). Equations (17), (18), and (4) form a set of equations that can be solved to yield the fractions of different types of nodes. The first two terms in Eqs. (17) and (18) correspond to the increase in inactive nodes due to failure and due to those remaining inactive, and the last term corresponds to recovery. The number of equations, again, depends on the choice of Δt. This is the mean-field approximation for the NMR model that ignores any spatial correlation.

Reporting summary. Further information on research design is available in the Nature Research Reporting Summary linked to this article.

Data availability
The source data underlying Figs. 2–7 and Supplementary Figs. 1–12 are available at https://github.com/zhlin2328/Codes-for-NCOMMS-19-1125220.

Code availability
C++ codes to reproduce the data in the main text and the Supplementary Information are available at https://github.com/zhlin2328/Codes-for-NCOMMS-19-1125220.

References
1. Motter, A. E. & Lai, Y.-C. Cascade-based attacks on complex networks. *Phys. Rev. E* **66**, 065102 (2002).
2. Zhao, L., Park, K. & Lai, Y.-C. Attack vulnerability of scale-free networks due to cascading breakdown. *Phys. Rev. E* **70**, 035101(R) (2004).
3. Zhao, L., Park, K., Lai, Y.-C. & Ye, N. Tolerance of scale-free networks against attack-induced cascades. *Phys. Rev. E* **72**, 025104(R) (2005).
4. Galstyan, A. & Cohen, P. Cascading dynamics in modular networks. *Phys. Rev. E* **75**, 036109 (2007).
5. Bialek, J. W. Why has it happened again? Comparison between the UCTE blackout in 2006 and the blackouts of 2003. In *Power Tech 2007 IEEE Lausanne* 51–56 (IEEE, 2007)
6. Dobson, I., Carreras, B. A., Lynch, V. E. & Newman, D. E. Complex systems analysis of series of blackouts: Cascading failure, critical points, and self-organization. *Chaos* **17**, 026103 (2007).
7. Gleeson, J. P. Cascades on correlated and modular random networks. *Phys. Rev. E* **77**, 046117 (2008).
8. Rosato, V. et al. Modelling interdependent infrastructures using interacting dynamical models. *Int. J. Crit. Infrastruct.* **4**, 63–79 (2008).
9. Huang, L., Lai, Y.-C. & Chen, G. Understanding and preventing cascading breakdown in complex clustered networks. *Phys. Rev. E* **78**, 036116 (2008).
10. Simonsen, I., Buzna, L., Peters, K., Bornholdt, S. & Helbing, D. Transient dynamics increasing network vulnerability to cascading failures. *Phys. Rev. Lett.* **100**, 218701 (2008).
11. Yang, R., Wang, W.-X., Lai, Y.-C. & Chen, G. Optimal weighting scheme for suppressing cascades and traffic congestion in complex networks. *Phys. Rev. E* **79**, 026112 (2009).
12. Takayasu, M., Watanabe, T. & Takayasu, H. *Econophysics Approaches to Large-Scale Business Data and Financial Crisis: Proceedings of Tokyo Tech-Hitotsubashi Interdisciplinary Conference and APFA7* (Springer, 2010)
13. Huang, L. & Lai, Y.-C. Cascading dynamics in complex quantum networks. *Chaos* **21**, 025107 (2011).
14. Wang, W., Lai, Y.-C. & Armbruster, D. Cascading failures and the emergence of cooperation in evolutionary-game based models of social and economical networks. *Chaos* **21**, 033112 (2011).
15. Liu, R.-R., Wang, W.-X., Lai, Y.-C. & Wang, B.-H. Cascading dynamics on random networks: crossover in phase transition. *Phys. Rev. E* **85**, 026110 (2012).
16. Li, D. et al. Percolation transition in dynamical traffic network with evolving critical bottlenecks. *Proc. Natl Acad. Sci. USA* **112**, 669–672 (2015).
17. Parshani, R., Buldyrev, S. V. & Havlin, S. Critical effect of dependency groups on the function of networks. *Proc. Natl Acad. Sci. USA* **108**, 1007–1010 (2011).
18. Watts, D. J. A simple model of global cascades on random networks. *Proc. Natl Acad. Sci. USA* **99**, 5766–5771 (2002).
19. Dodds, P. S. & Watts, D. J. Universal behavior in a generalized model of contagion. *Phys. Rev. Lett.* **92**, 218701 (2004).
20. Simonsen, I., Buzna, L., Peters, K., Bornholdt, S. & Helbing, D. Transient dynamics increasing network vulnerability to cascading failures. *Phys. Rev. Lett.* **100**, 218701 (2008).
21. Buldyrev, S. V., Parshani, R., Paul, G., Stanley, H. E. & Havlin, S. Catastrophic cascade of failures in interdependent networks. *Nature* **464**, 1025 (2010).
22. Ganin, A. A. et al. Resilience and efficiency in transportation networks. *Sci. Adv.* **3**, e1701079 (2017).
23. Nudo, R. J. Recovery after brain injury: mechanisms and principles. *Front. Hum. Neurosci.* **7**, 887 (2013).
24. Shang, Y. Impact of self-healing capability on network robustness. *Phys. Rev. E* **91**, 042804 (2015).
25. Hu, F., Yeung, C. H., Yang, S., Wang, W. & Zeng, A. Recovery of infrastructure networks after localised attacks. *Sci. Rep.* **6**, 24522 (2016).
26. White, S. R. et al. Autonomic healing of polymer composites. *Nature* **409**, 794 (2001).
27. Toohey, K. S., Sottos, N. R., Lewis, J. A., Moore, J. S. & White, S. R. Self-healing materials with microvascular networks. *Nat. Mater.* **6**, 581 (2007).
28. Desmurget, M., Bonnetblanc, F. & Duffau, H. Contrasting acute and slow-growing lesions: a new door to brain plasticity. *Brain* **130**, 898–914 (2007).
29. Majdandzic, A. et al. Spontaneous recovery in dynamical networks. *Nat. Phys.* **10**, 34 (2014).
30. Podobnik, B. et al. Network risk and forecasting power in phase-flipping dynamical networks. *Phys. Rev. E* **89**, 042807 (2014).
31. Podobnik, B. et al. Predicting the lifetime of dynamic networks experiencing persistent random attacks. *Sci. Rep.* **5**, 14286 (2015).
32. Podobnik, B. et al. The cost of attack in competing networks. *J. R. Soc. Interface* **12**, 20150770 (2015).
33. Majdandzic, A. et al. Multiple tipping points and optimal repairing in interacting networks. *Nat. Commun.* **7**, 10850 (2016).
34. Council, N. R. et al. *Disaster Resilience: A National Imperative* (The National Academies Press, Washington DC, 2012).
35. Gao, J., Barzel, B. & Barabási, A.-L. Universal resilience patterns in complex networks. *Nature* **530**, 307–312 (2016).
36. Ganin, A. A. et al. Operational resilience: concepts, design and analysis. *Sci. Rep.* **6**, 1–12 (2016).
37. Linkov, I. & Trump, B. D. *The Science and Practice of Resilience* (Springer, 2019)
38. Pastor-Satorras, R., Castellano, C., Van Mieghem, P. & Vespignani, A. Epidemic processes in complex networks. *Rev. Mod. Phys.* **87**, 925 (2015).

39. Wang, W., Tang, M., Stanley, H. E. & Braunstein, L. A. Unification of theoretical approaches for epidemic spreading on complex networks. *Rep. Prog. Phys.* **80**, 036603 (2017).

40. de Arruda, G. F., Rodrigues, F. A. & Moreno, Y. Fundamentals of spreading processes in single and multilayer complex networks. *Phys. Rep.* **756**, 1–60 (2018).

41. Barabasi, A.-L. The origin of bursts and heavy tails in human dynamics. *Nature* **435**, 207 (2005).

42. González, M. C., Hidalgo, C. A. & Barabási, A. L. Understanding individual human mobility patterns. *Nature* **453**, 779–782 (2008).

43. Simini, F., González, M. C., Maritan, A. & Barabási, A. L. A universal model for mobility and migration patterns. *Nature* **484**, 96–100 (2012).

44. Zhao, Z.-D. et al. Emergence of scaling in human-interest dynamics. *Sci. Rep.* **3**, 3472 (2013).

45. Zhao, Z.-D., Huang, Z.-G., Huang, L., Liu, H. & Lai, Y.-C. Scaling and correlation of human movements in cyber and physical spaces. *Phys. Rev. E* **90**, 050802(R) (2014).

46. Pappalardo, L. et al. Returners and explorers dichotomy in human mobility. *Nat. Commun.* **6**, 8166 (2015).

47. Zhao, Y.-M., Zeng, A., Yan, X.-Y., Wang, W.-X. & Lai, Y.-C. Unified underpinning of human mobility in the real world and cyberspace. *N. J. Phys.* **18**, 053025 (2016).

48. Yan, X.-Y., Wang, W.-X., Gao, Z.-Y. & Lai, Y.-C. Universal model of individual and population mobility on diverse spatial scales. *Nat. Commun.* **8**, 1639 (2017).

49. Bratsun, D., Volfson, D., Tsimring, L. S. & Hasty, J. Delay-induced stochastic oscillations in gene regulation. *Proc. Natl Acad. Sci. USA* **102**, 14593–14598 (2005).

50. Scalas, E., Kaizoji, T., Kirchler, M., Huber, J. & Tedeschi, A. Waiting times between orders and trades in double-auction markets. *Phys. A* **366**, 463–471 (2006).

51. Vazquez, A., Racz, B., Lukacs, A. & Barabasi, A.-L. Impact of non-Poissonian activity patterns on spreading processes. *Phys. Rev. Lett.* **98**, 158702 (2007).

52. Iribarren, J. L. & Moro, E. Impact of human activity patterns on the dynamics of information diffusion. *Phys. Rev. Lett.* **103**, 038702 (2009).

53. Van Mieghem, P. & Van de Bovenkamp, R. Non-Markovian infection spread dramatically alters the susceptible-infected-susceptible epidemic threshold in networks. *Phys. Rev. Lett.* **110**, 108701 (2013).

54. Jo, H.-H., Perotti, J. I., Kaski, K. & Kertész, J. Analytically solvable model of spreading dynamics with non-Poissonian processes. *Phys. Rev. X* **4**, 011041 (2014).

55. Kiss, I. Z., Röst, G. & Vizi, Z. Generalization of pairwise models to non-Markovian epidemics on networks. *Phys. Rev. Lett.* **115**, 078701 (2015).

56. Starnini, M., Gleeson, J. P. & Boguñá, M. Equivalence between non-Markovian and Markovian dynamics in epidemic spreading processes. *Phys. Rev. Lett.* **118**, 128301 (2017).

57. Sherborne, N., Miller, J., Blyuss, K. & Kiss, I. Mean-field models for non-Markovian epidemics on networks. *J. Math. Biol.* **76**, 755–558 (2018).

58. Feng, M., Cai, S.-M., Tang, M. & Lai, Y.-C. Equivalence and its invalidation between non-Markovian and Markovian spreading dynamics on complex networks. *Nat. Commun.* **10**, 3748 (2019).

59. Valdez, L. D., DiMuro, M. A. & Braunstein, L. A. Failure-recovery model with competition between failures in complex networks: a dynamical approach. *J. Stat. Mech.* **2016**, 093402 (2016)

60. Böttcher, L., Nagler, J. & Herrmann, H. J. Critical behaviors in contagion dynamics. *Phys. Rev. Lett.* **118**, 1–5 (2017).

61. Böttcher, L., Luković, M., Nagler, J., Havlin, S. & Herrmann, H. J. Failure and recovery in dynamical networks. *Sci. Rep.* **7**, 41729 (2017).

62. Keeling, M., Rand, D. & Morris, A. Correlation models for childhood epidemics. *Proc. R. Soc. Lond. Ser. B* **264**, 1149–1156 (1997).

63. benAvraham, D. & Köhler, J. Mean-field (n, m)-cluster approximation for lattice models. *Phys. Rev. A* **45**, 8358 (1992).

64. Mata, A. S. & Ferreira, S. C. Pair quenched mean-field theory for the susceptible-infected-susceptible model on complex networks. *EPL* **103**, 48003 (2013).

65. Gross, T., D'Lima, C. J. D. & Blasius, B. Epidemic dynamics on an adaptive network. *Phys. Rev. Lett.* **96**, 208701 (2006).

66. Ji, M., Xu, C., Choi, C. W. & Hui, P. M. Correlation and analytic approaches to co-evolving voter models. *N. J. Phys.* **15**, 113024 (2013).

67. Zhang, W., Xu, C. & Hui, P. M. Spatial structure enhanced cooperation in dissatisfied adaptive snowdrift game. *Eur. Phys. J. B* **86**, 196 (2013).

68. Zhang, W., Li, Y. S., Du, P., Xu, C. & Hui, P. M. Phase transitions in a coevolving snowdraft game with costly rewiring. *Phys. Rev. E* **90**, 052819 (2014).

69. Choi, C. W., Xu, C. & Hui, P. M. Adaptive cyclically dominating game on co-evolving networks: numerical and analytic reuslts. *Eur. Phys. J. B* **90**, 190 (2017).

70. Harris, S. *An Introduction to the Theory of the Boltzmann Equation* (Courier Corporation, 2004)

Acknowledgements

Author contributions
Z.-H.L., M.T., and Z.H.L. designed research; Z.-H.L. performed research; Z.-H.L., M.F., M.T., Z.H.L., C.X., and P.M.H. contributed analytic tools; Z.-H.L., M.F., M.T., Z.H.L., C.X., P.M.H., and Y.-C.L. analyzed data; Z.-H.L., M.T., Z.H.L., P.M.H., and Y.-C.L. wrote the paper.

Competing interests
The authors declare no competing interests.

Additional information

Supplementary Information for

Non-Markovian recovery makes complex networks more resilient against large scale failures

Zhao-Hua Lin, Mi Feng, Ming Tang, Zonghua Liu, Chen Xu, Pak Ming Hui and Ying-Cheng Lai

Corresponding author: Ming Tang (tangminghan007@gmail.com), Zonghua Liu(zhliu@phy.ecnu.edu.cn)

CONTENTS

I. SUPPLEMENTARY FIGURES

Supplementary Figure 1. **Effects of initial conditions on phase transition**. The initial conditions are $[X]_0 \neq 0$ and $[Y]_0 = 0$. The phase transition is with respect to a systematic increase in the value of parameter β_1. The results are obtained from the same initial conditions for different values of β_1 (for a fixed β_2 value). There is a critical value $\beta_c([X]_0)$ beyond which the system approaches a high-failure state. (a,b) Results for MR and NMR models, respectively, where the blue circles, orange down triangles, green pentagons, red up triangles, purple diamonds represent the results from different initial fractions of failed nodes: $[X]_0 = 0.01, 0.1, 0.23, 0.25, 0.99$, respectively. Other parameters are $\beta_2 = 2$, $\mu_1 = 0.01$, $\mu_2 = 1$, $\tau_1 = 100$, $\tau_2 = 1$, and $m = 15$. The network has a random regular structure with size $N = 3 \times 10^4$ and nodal degree $k = 35$.
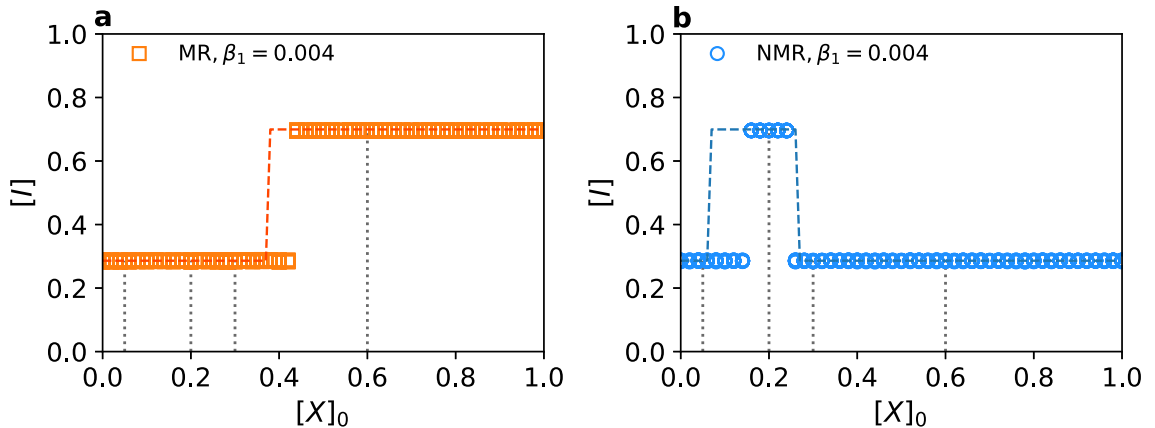
Supplementary Figure 2. **Effects of initial conditions on stationary solution**. The initial conditions are $[X]_0 \neq 0$ and $[Y]_0 = 0$. The stationary solution $[I]$ is obtained for $\beta_1 = 0.004$ for MR (a) and NMR (b) models. Orange squares and blue circles are simulation results for MR and NMR models, respectively. The dashed line represents the mean-field prediction. The gray dotted vertical lines correspond to $[X]_0 = 0.05, 0.2, 0.3, 0.6$, respectively.

2
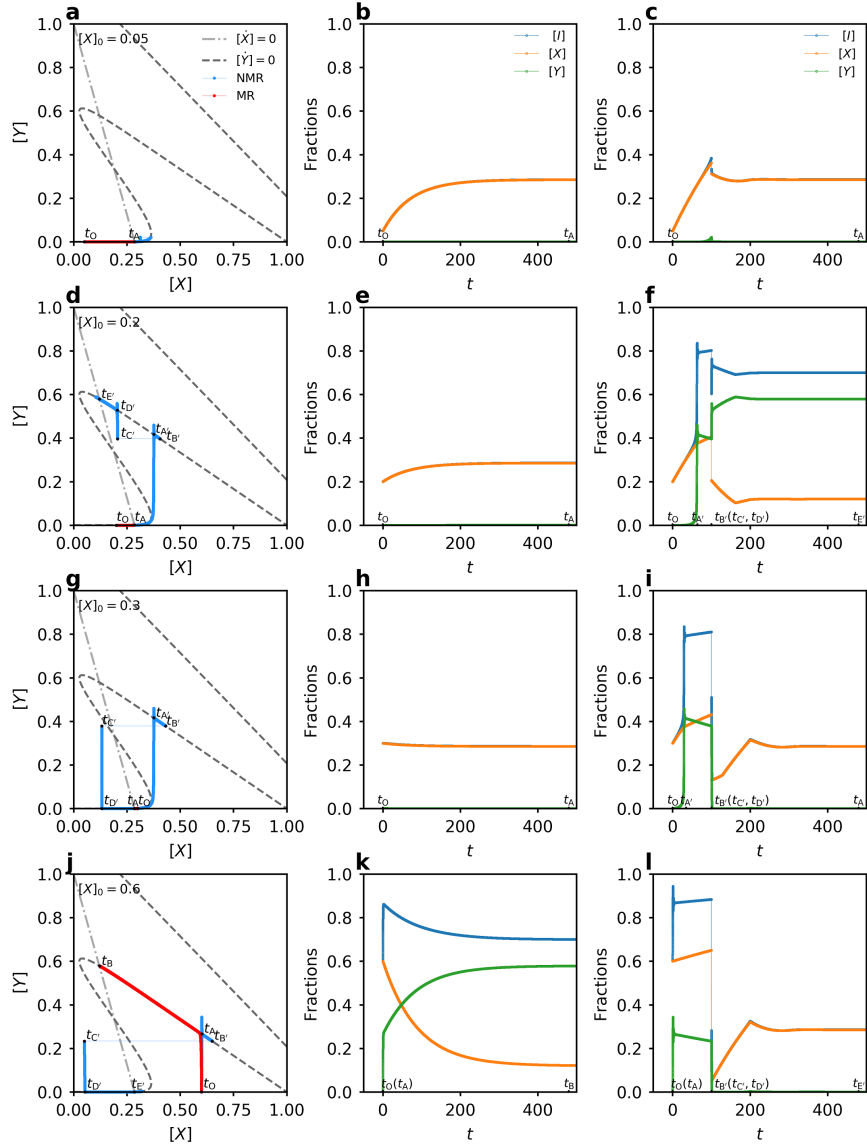
Supplementary Figure 3. **Trajectories and time evolution of fractions of X-type and Y-type nodes**. The initial conditions are $[X]_0 \neq 0$ and $[Y]_0 = 0$. The results are obtained from the mean-field theory. For fixed $[X]_0 = 0.05$, (a) trajectories of $[X]$ and $[Y]$, (b,c) time evolution from the MR and NMR models, respectively. (d-f) The corresponding results for $[X]_0 = 0.2$. (g-i) The results for $[X]_0 = 0.3$. (j-l) The results for $[X]_0 = 0.6$. The solid blue and red lines in the first column are the results from the NMR and MR models, respectively. The light and dark gray dotted lines are the solutions of $[\dot{X}] = 0$ and $[\dot{Y}] = 0$ from the mean-field theory for the MR model, respectively, where their intersections give the steady-state solutions. The solid blue, orange and green lines in the second and third columns are the results of $[I]$, $[X]$ and $[Y]$ for the MR and NMR models, respectively. The evolution from $t_{B'}$ to $t_{C'}$ and then to $t_{D'}$ is too fast to be distinguished in (f), (i) and (l). The evolution from t_O to t_A is also too short for it to be seen in (k) and (l). Other parameter values are $\beta_1 = 0.004$, $\beta_2 = 2$, $\mu_1 = 0.01$, $\mu_2 = 1$, $\tau_1 = 100$, $\tau_2 = 1$, and $m = 15$. The network is the same as that in Supplementary Fig. 1.

3
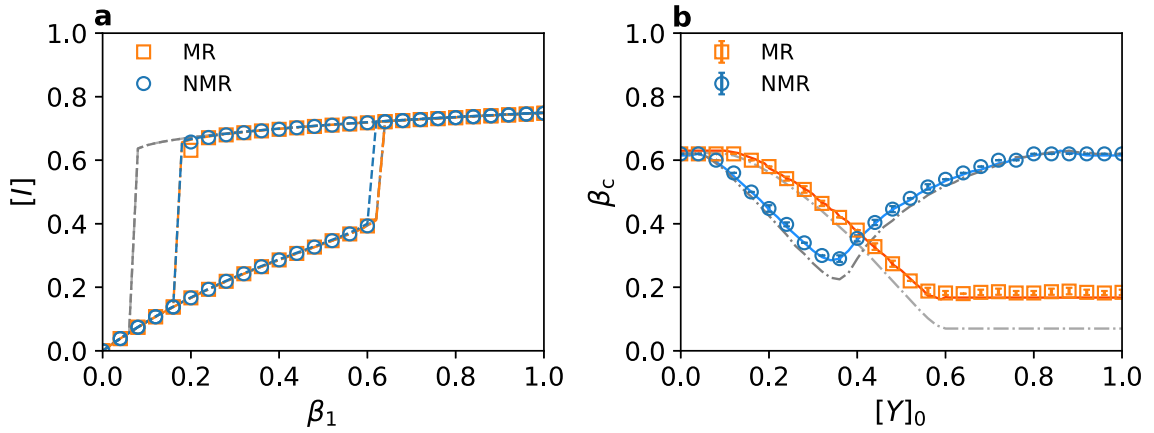
Supplementary Figure 4. **MR and NMR dynamics in situations where external recovery is slower than internal recovery**. (a) Dependence of $[I]$ on β_1 in the steady state for $\beta_2 = 0.1$, $\tau_1 = 1.0$ (corresponding to $\mu_1 = 1.0$), $\tau_2 = 20$ (corresponding to $\mu_2 = 0.05$), and $m = 15$. Orange squares (blue circles) are simulation results for the MR (NMR) model. The results are averaged for two network configurations, each of ten realizations. The orange dot-dashed (blue dashed) line is calculated by the PA theory for the MR (NMR) model. The gray dot-dashed (dashed) line is the result from the MF theory for the MR (NMR) model. (b) Dependence of β_c on the initial value of $[Y]_0$, with $[X]_0 = 0$. The solid (dot-dashed) lines are obtained from the PA (MF) theory. The networks are RRNs with $N = 30000$ and $k = 35$.
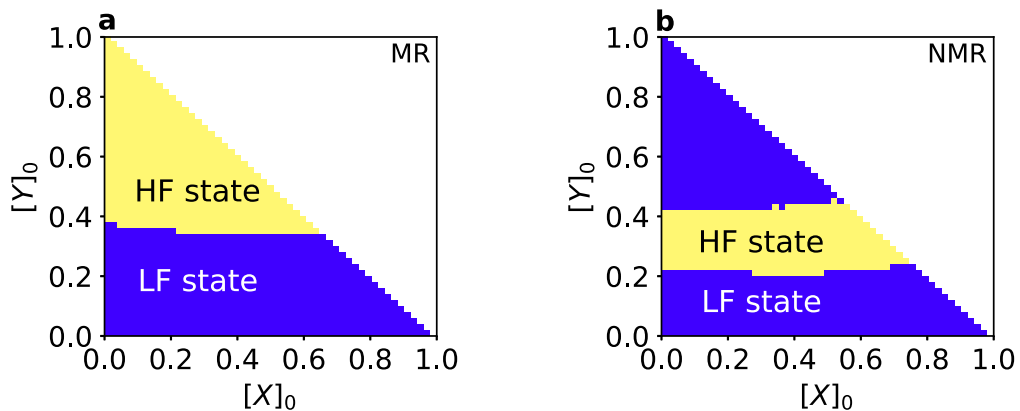
Supplementary Figure 5. **Basin structures**. On the $[X]_0$-$[Y]_0$ plane, basin structure for (a) MR and (b) NMR model for $\beta_1 = 0.4$, where the colors indicate the nature of the steady states from different initial conditions. Other parameters are the same as those in Supplementary Fig. 4.

4
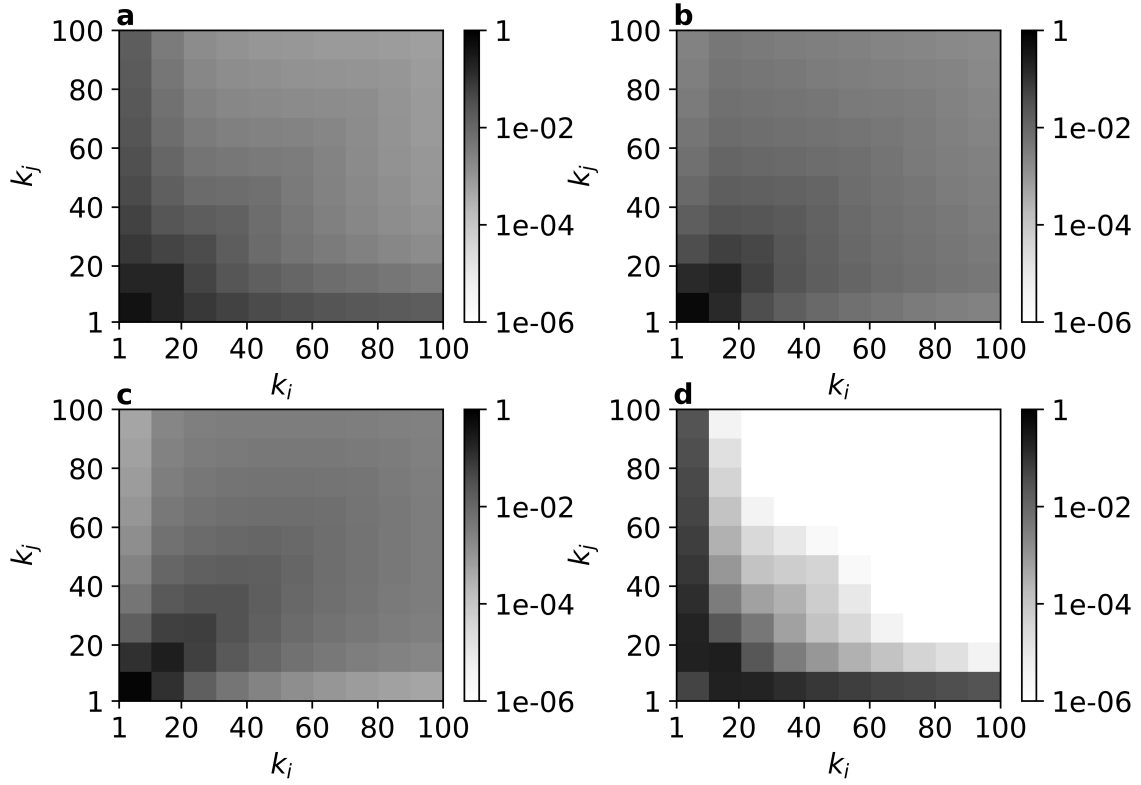
Supplementary Figure 6. **Visualizations of degree-degree correlation in a network**. Shading colors of the matrix correspond to the probabilities that a randomly chosen edge connects nodes i of degree k_i and j of k_j, where the results are averaged with 100 UCN realizations for (a) $r = 0$, (b) $r = 0.5$, (c) $r = 0.7$ and (d) $r = -0.5$. Each grid cell represents the average result with the degree range of ten for visualization. Other network parameters are $N = 10000$, $\gamma = 2.5$, $k_{\min} = 5$, and $k_{\max} = 100$.
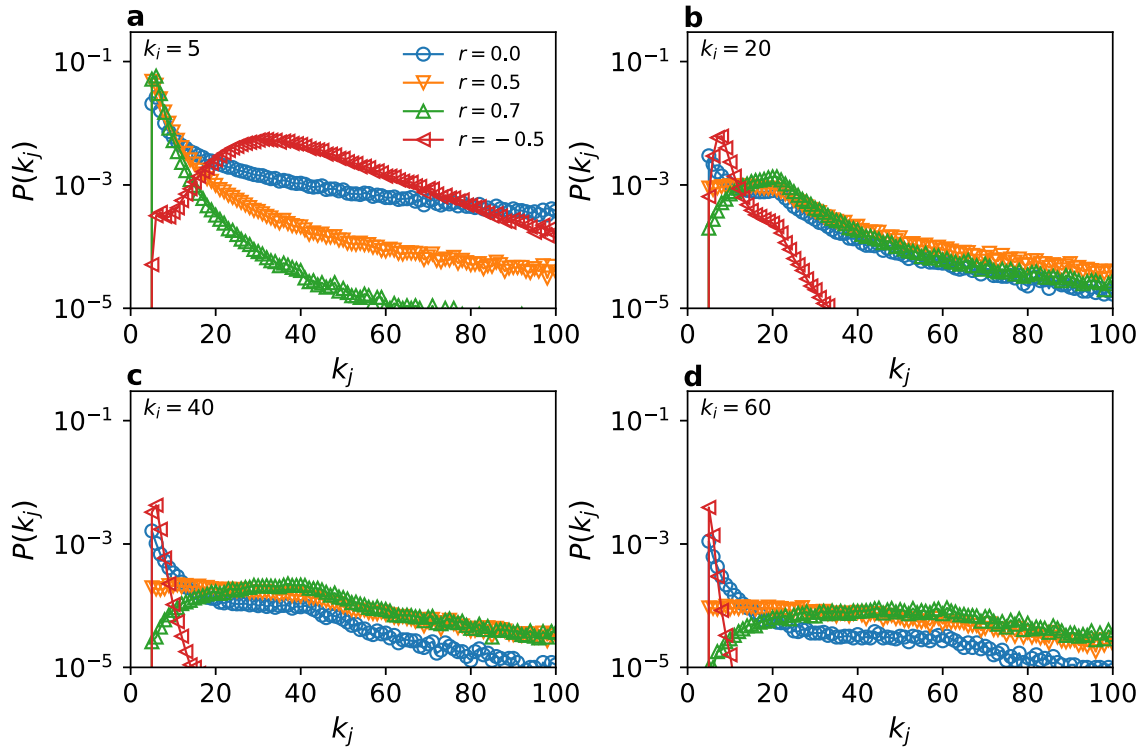
Supplementary Figure 7. **Probability distribution of a node of degree k_i connecting to a node of degree k_j.** (a-d): node i of degree $k_i = 5$, $k_i = 20$, $k_i = 40$ and $k_i = 60$, respectively. Blue circles, orange down triangles, green up triangles and red left triangles are the results for different level of degree-degree correlation $r = 0$, $r = 0.5$, $r = 0.7$ and $r = -0.5$ in Supplementary Figs. 6, respectively.
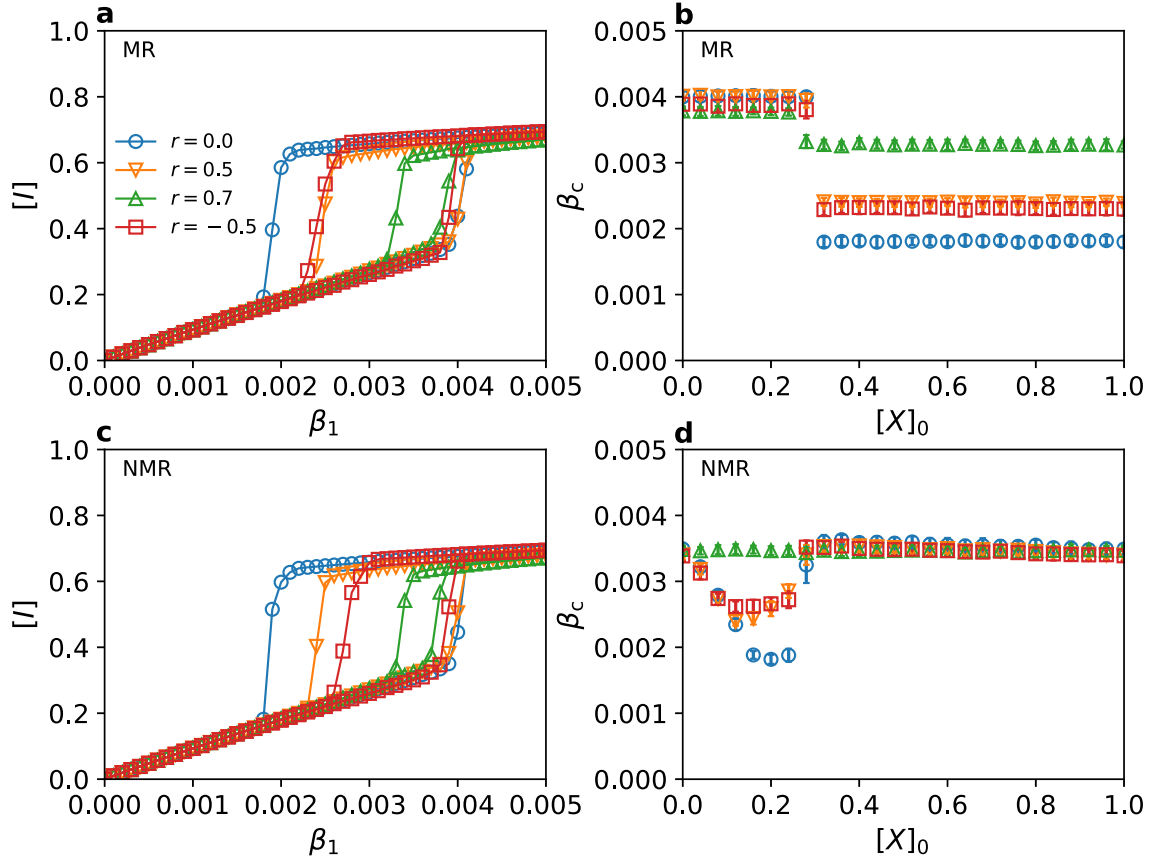
Supplementary Figure 8. **MR and NMR dynamics in UCNs with degree-degree correla-
tion**. (a) Dependence of $[I]$ on β_1 in the steady state for the MR model. The parameter values are
$\beta_2 = 2.0$, $\tau_1 = 100$ (corresponding to $\mu_1 = 0.01$), and $\tau_2 = 1.0$ (corresponding to $\mu_2 = 1.0$). The
threshold of external failure of a node is that half of its neighbors have failed. Blue circles, orange
down triangles, green up triangles and red squares are the simulation results for different values
of the degree-degree correlation coefficient: $r = 0$, $r = 0.5$, $r = 0.7$ and $r = -0.5$, respectively.
(b) Dependence of β_c on the initial value of $[X]_0$ for the MR model for $[Y]_0 = 0$. (c,d) Simulation
results averaged over 50 realizations for the NMR model. The networks are of the UCM type with
$N = 10000$, $k_{min} = 5$, $k_{max} = 100$, and different levels of degree-degree correlation.

7
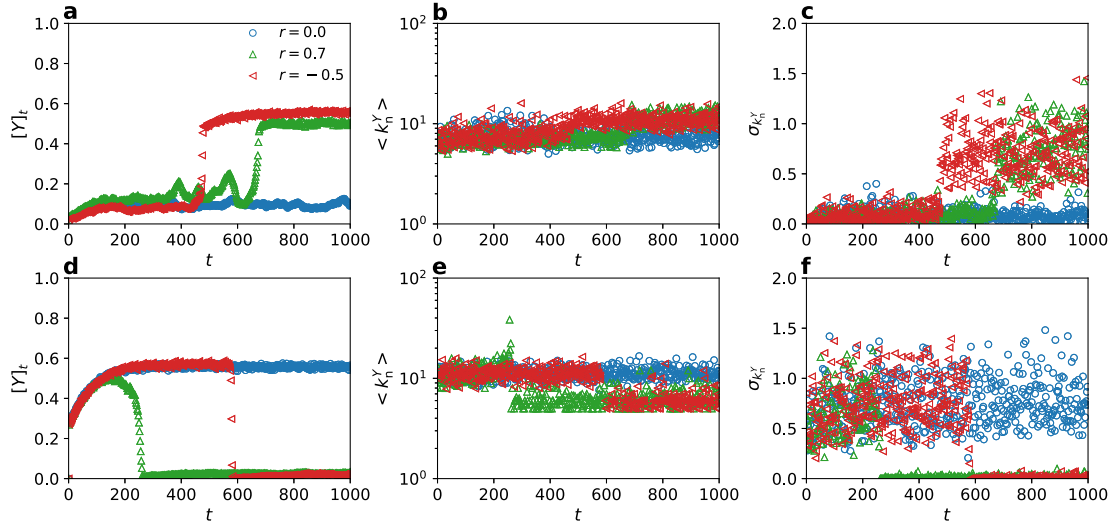
Supplementary Figure 9. **Dynamical behaviors on UCNs with different levels of degree-degree correlation for the MR model**. (a,d) Time evolution of the fraction of Y-type nodes. Blue circles, green up triangles and red left triangles are for $r = 0$, $r = 0.7$ and $r = -0.5$, respectively. (b,e) Time evolution of the average degree of newly emerged Y-type nodes. (c,f) Variance of the newly emerged Y-type nodes whose degrees correspond to those in Supplementary Fig. 9(b). (a-c): Results for $\beta_1 = 0.004$ and $[X]_0 = 0.2$. (d-f) Results for $\beta_1 = 0.0022$ and $[X]_0 = 0.6$. A single realization is used here for better visualization. Other parameter values are the same as those in Supplementary Fig. 8.
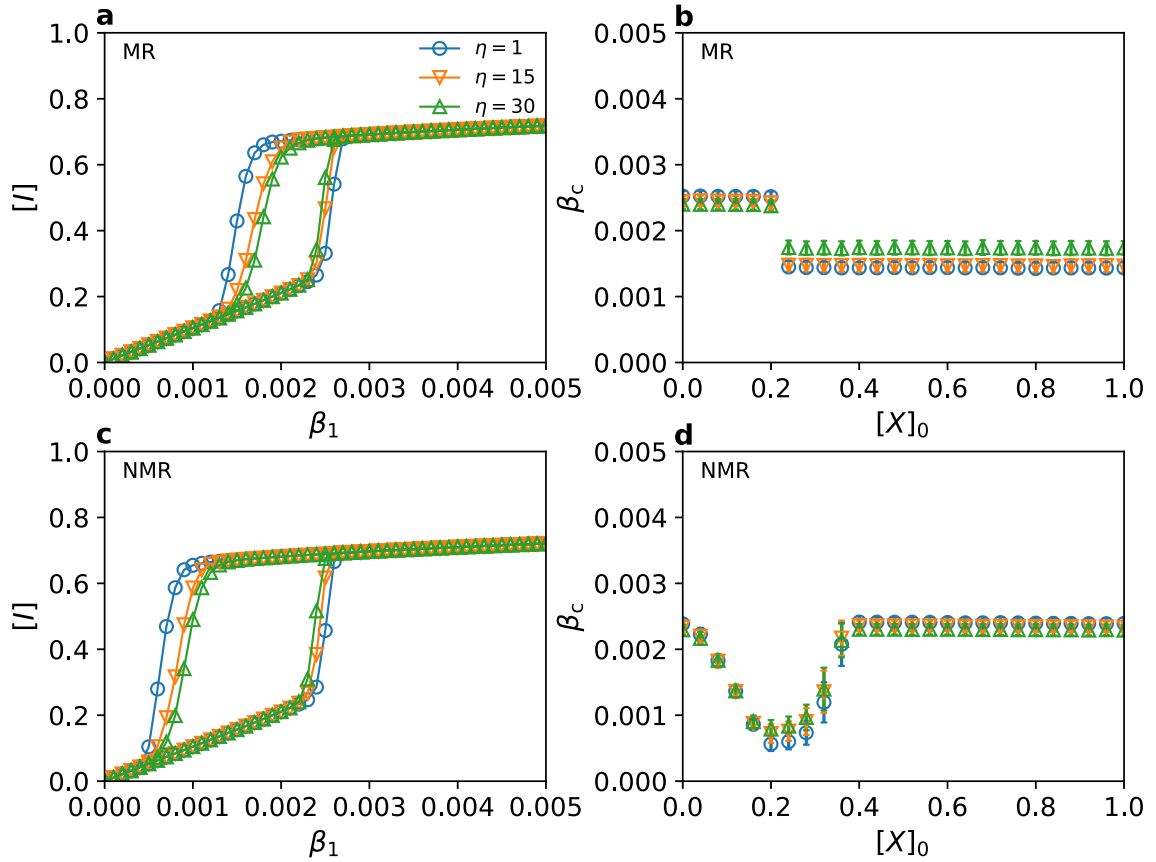
Supplementary Figure 10. **MR and NMR dynamics in networks with a community struc-ture**. (a) Dependence of $[I]$ on β_1 in the steady state for the MR model for $\beta_2 = 2.4$. Blue circles, orange down triangles and green up triangles are simulation results for $Q \approx -0.01$, $Q = 0.43$ and $Q = 0.46$, respectively. Each data point is the result of averaging over 20 network realizations, each with 50 random initial conditions. (b) Dependence of β_c on the initial value of $[X]_0$ for the MR model for $[Y]_0 = 0$. (c,d) The corresponding simulation results for the NMR model. The network size is $N = 3000$ and the mean degree is $\langle k \rangle = 6$. Other parameters are the same as those in Supplementary Fig. 8.
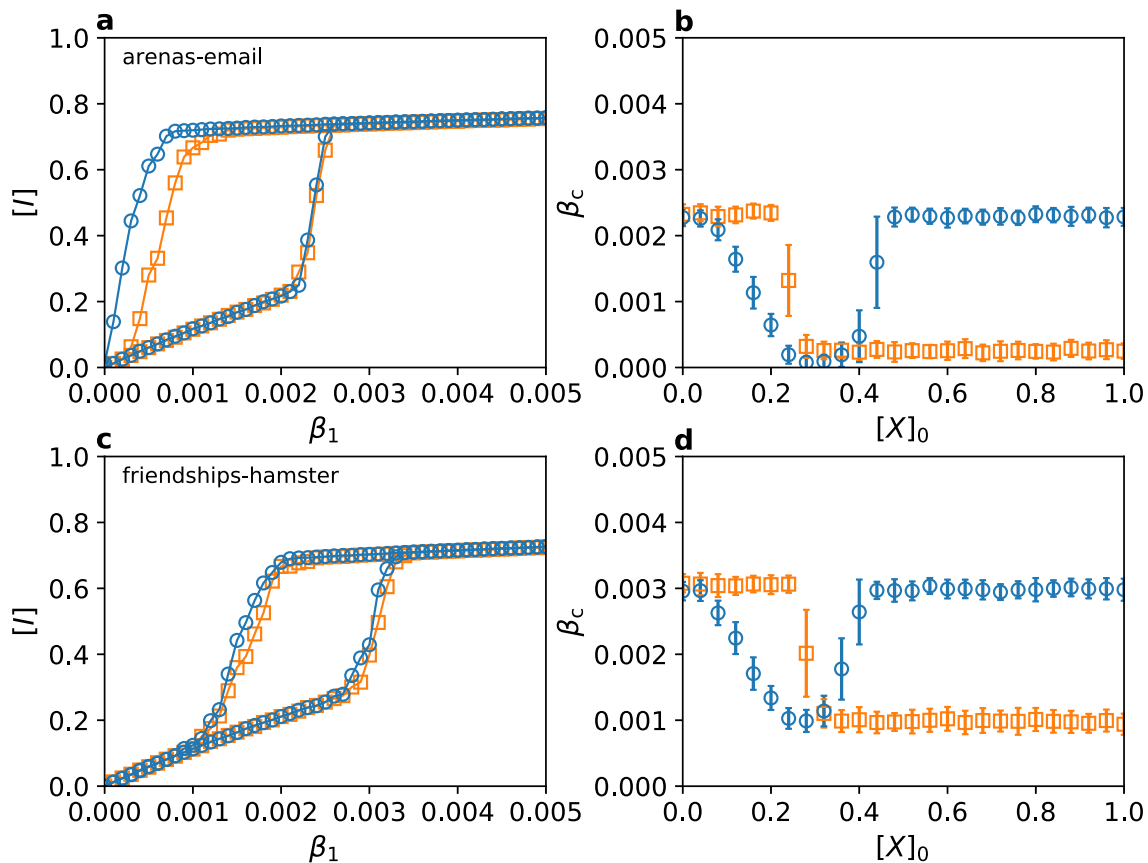
Supplementary Figure 11. **Comparison between MR and NMR dynamics in the empirical networks**. (a) Dependence of $[I]$ on β_1 in the steady state in the arenas-email network for $\beta_2 = 2.9$. Blue circles and orange squares are simulation results averaged over 50 realizations for the MR and NMR dynamical models, respectively. (b) Dependence of β_c on the initial value of $[X]_0$ for the MR and NMR models for $[Y]_0 = 0$. (c,d) The corresponding results in the friendship-hamster network for $\beta_2 = 2.5$. Other parameters are the same as those in Supplementary Fig. 8.
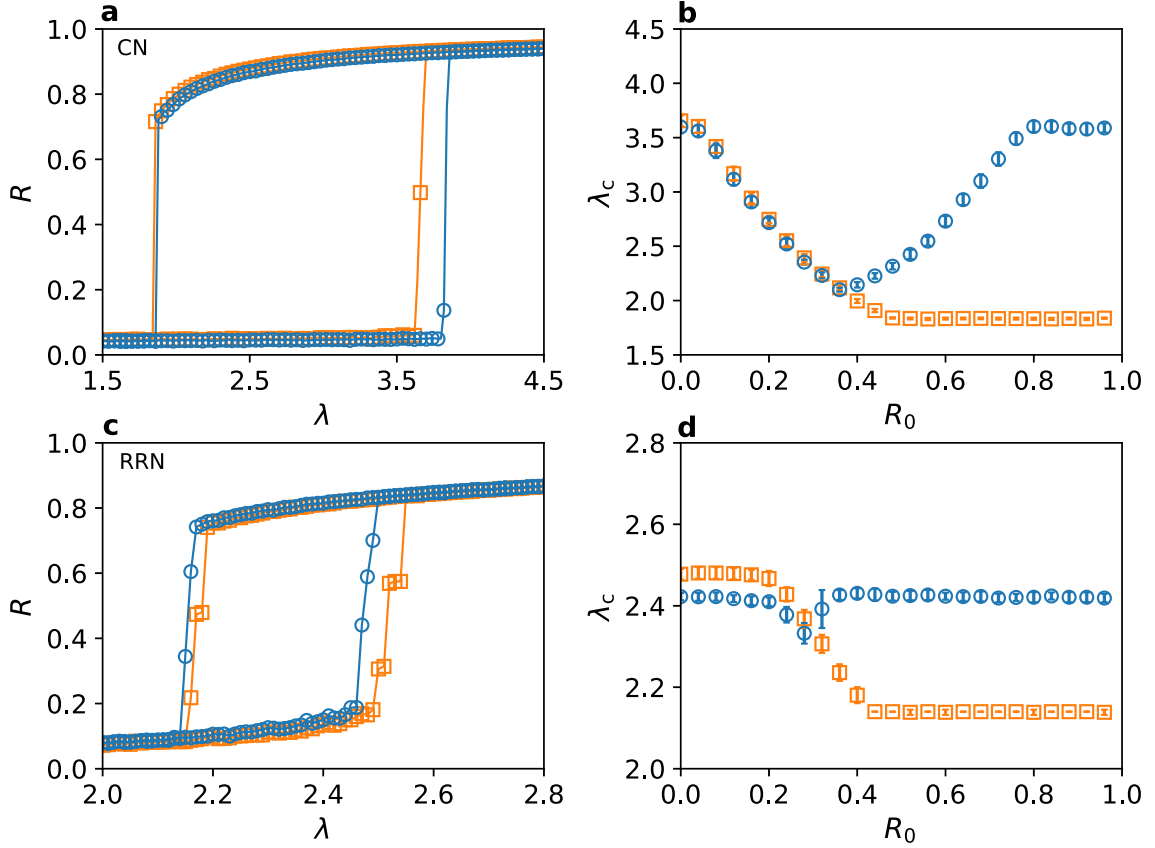
Supplementary Figure 12. **MR and NMR dynamics for power-grid synchronization**. (a,c) Dependence of order parameter R on the coupling strength λ in the steady state for a completely connected network (CN) and a random regular network (RRN), respectively. The results are averaged over 20 realizations. (b,d) Dependence of λ_c on the initial order parameter R_0 for the CN and RRN, respectively. Blue circles and orange squares are for the NMR and MR model, respectively. Other parameters are $a = 0.05$, $p = 0.01$, $\omega_0 = 0$, $\Delta = 0.5$, $\phi = 0$, $\psi = \pi/4$, $N = 5000$, and $\langle k \rangle = 10$ (for RRN).

II. SUPPLEMENTARY NOTES

A. Supplementary Note 1: Pairwise approximation theory

1. Markovian recovery model

We use symbols of the forms $[U]_t$ and $[UV]_t$ with $U, V \in \{A, X, Y\}$ to denote the fractions of nodes and edges in different states at time t, respectively. For example, $[A]_t$, $[X]_t$ and $[Y]_t$ represent the fractions of active nodes, X-type and Y-type failed nodes at time t, respectively, whereas $[AX]_t$ stands for the fraction of active nodes connected with an X-type failed node (i.e., the fraction of AX-type links) at time t. Taking into account every link from every node, the link fractions satisfy the "conservation law": $\sum_{U,V \in \{A,X,Y\}}[UV]_t = 1$, with $[UV]_t = [VU]_t$ for $U \neq V$. The supplementary evolution equations for the fractions of

11

various types of nodes and edges are given by

$$\frac{d[A]_t}{dt} = \mu_1[X]_t + \mu_2[Y]_t - (\beta_1 + \beta_2 E_t)[A]_t, \tag{1}$$

$$\frac{d[X]_t}{dt} = \beta_1[A]_t - \mu_1[X]_t, \tag{2}$$

$$\frac{d[Y]_t}{dt} = \beta_2 E_t[A]_t - \mu_2[Y]_t, \tag{3}$$

$$\frac{d[AX]_t}{dt} = \mu_1[XX]_t + \mu_2[YX]_t + \beta_1[AA]_t - \mu_1[AX]_t - (\beta_1 + \beta_2 E'_{x,t})[AX]_t, \tag{4}$$

$$\frac{d[AY]_t}{dt} = \mu_1[XY]_t + \mu_2[YY]_t + \beta_2 E''_t[AA]_t - \mu_2[AY]_t - (\beta_1 + \beta_2 E'_{y,t})[AY]_t, \tag{5}$$

$$\frac{d[AA]_t}{dt} = \mu_1([XA]_t + [AX]_t) + \mu_2([YA]_t + [AY]_t) - 2(\beta_1 + \beta_2 E''_t)[AA]_t, \tag{6}$$

$$\frac{d[YY]_t}{dt} = \beta_2 E'_{y,t}([AY]_t + [YA]_t) - 2\mu_2[YY]_t, \tag{7}$$

$$\frac{d[XX]_t}{dt} = \beta_1([AX]_t + [XA]_t) - 2\mu_1[XX]_t, \tag{8}$$

$$\frac{d[XY]_t}{dt} = \beta_1[AY]_t + \beta_2 E'_{x,t}[XA]_t - (\mu_1 + \mu_2)[XY]_t, \tag{9}$$

where

$$E_t = \sum_{j=0}^{m} C_k^{k-j} \left(\frac{[AI]_t}{[A]_t}\right)^{k-j} \left(1 - \frac{[AI]_t}{[A]_t}\right)^j, \tag{10}$$

$$E'_{x,t} = \sum_{j=0}^{m} C_{k-1}^{k-1-j} \left(\frac{[IAX]_t}{[AX]_t}\right)^{k-1-j} \left(1 - \frac{[IAX]_t}{[AX]_t}\right)^j, \tag{11}$$

$$E'_{y,t} = \sum_{j=0}^{m} C_{k-1}^{k-1-j} \left(\frac{[IAY]_t}{[AY]_t}\right)^{k-1-j} \left(1 - \frac{[IAY]_t}{[AY]_t}\right)^j, \tag{12}$$

$$E''_t = \sum_{j=0}^{m-1} C_{k-1}^{k-1-j} \left(\frac{[IAA]_t}{[AA]_t}\right)^{k-1-j} \left(1 - \frac{[IAA]_t}{[AA]_t}\right)^j. \tag{13}$$

In the supplementary evolution equation of $[X]_t$ ($[Y]_t$), the first term represents the fraction of failed A-type nodes due to an internal (external) mechanism, which increases the fraction of the X-type (Y-type) nodes. The second term describes the transition that X-type (Y-type) nodes recover, which decreases the fraction of the X-type (Y-type) nodes.

In the supplementary equation of $[AX]_t$, the first (second) term represents the transition that an X-type (Y-type) node connected with an X-type failed node recovers spontaneously (i.e., become again an A-type node), which increases the fraction of AX edges. The third term represents the situation that the A-type neighbors of the A-type nodes fail due to an internal mechanism, which increases the fraction of AX edges. The forth term describes the transition that X-type nodes at the ends of AX edges recover spontaneously, which decreases

12

the fraction of AX edges. The last term represents the transition that A-type nodes at the ends of AX edges fail due to an internal or an external mechanism, which decreases the fraction of AX edges. In the supplementary equation of $[AA]_t$, the first (second) term represents the transition that X-type (Y-type) nodes at the ends of AX and XA (AY and YA) edges recover spontaneously, which increases the fraction of AA edges. The third term represents the transition that A-type nodes at the ends of AA edges fail due to the an internal or an external cause (i.e., become X-type or Y-type nodes), which decreases the fraction of AA edges.

From the set of supplementary equations, we see that, under different conditions, the probabilities of an active node satisfying the threshold condition are different. We use the notations E_t, $E'_{x,t}$, $E'_{y,t}$ and E''_t for various probabilities: E_t is the probability for an active node to satisfy the threshold condition, $E'_{x,t}$ ($E'_{y,t}$) is the probability for an A-type node associated with an AX (AY) edge to satisfy the threshold condition, and E''_t denotes the probability that an A-type node connected with an A-type node satisfies the threshold condition. For all the probabilities, the threshold condition is $n_A \leq m$, where n_A is the number of active neighbors.

Using the pairwise approximation

$$[UVW]_t = \frac{[UV]_t[VW]_t}{[V]_t}, \tag{14}$$

we have

$$\frac{[IAX]_t}{[AX]_t} = \frac{[AI]_t}{[A]_t}, \tag{15}$$

$$\frac{[IAY]_t}{[AY]_t} = \frac{[AI]_t}{[A]_t}, \tag{16}$$

and

$$\frac{[IAA]_t}{[AA]_t} = \frac{[AI]_t}{[A]_t}, \tag{17}$$

i.e., $E'_{x,t} = E'_{y,t}$. Letting $E'_{x,t} = E'_{y,t} = E'_t$, we have

$$E_t = \sum_{j=0}^{m} C_k^{k-j} \left(\frac{[AI]_t}{[A]_t} \right)^{k-j} \left(1 - \frac{[AI]_t}{[A]_t} \right)^j, \tag{18}$$

$$E'_t = \sum_{j=0}^{m} C_{k-1}^{k-1-j} \left(\frac{[AI]_t}{[A]_t} \right)^{k-1-j} \left(1 - \frac{[AI]_t}{[A]_t} \right)^j, \tag{19}$$

and

$$E''_t = \sum_{j=0}^{m-1} C_{k-1}^{k-1-j} \left(\frac{[AI]_t}{[A]_t} \right)^{k-1-j} \left(1 - \frac{[AI]_t}{[A]_t} \right)^j. \tag{20}$$

Altogether, in the MR model, Supplementary Eqs. (1-9) describe the failure propagation dynamics.

13

To capture the memory effect of the NMR process, we write the model in terms of supplementary difference equations by decomposing the NMR process into a series of MR processes. In the following, each supplementary difference equations describes the relationship among the fractions of nodes or edges in different states at time $t + \Delta t$ and time t. We invoke the notations $[U]_t$ and $[UV]_t$ with $U, V \in \{A, X, Y\}$ to represent the fractions of nodes and edges of different types at time t, respectively. In addition, we use the notations $[U^l]_t$, $[U^{l_1}V^{l_2}]_t$ and $[U^lV]_t$, where l, l_1 and l_2 represent the passing time of the corresponding nodes being in the current state at time t. Due to symmetry, we have $[AX]_t = [XA]_t$. The supplementary evolutionary equations of the NMR model are given by

$$[A]_{t+\Delta t} = [X^{\tau_1}]_t + [Y^{\tau_2}]_t + (1 - \beta_1 \Delta t - \beta_2 \Delta t E_t)[A]_t, \tag{21}$$

$$[X^l]_{t+\Delta t} = \begin{cases} \beta_1 \Delta t [A]_t, & l \in [0, \Delta t); \\ [X^{l-\Delta t}]_t, & l \in [\Delta t, \tau_1]; \\ 0, & l \in (\tau_1, \infty), \end{cases} \tag{22}$$

$$[Y^l]_{t+\Delta t} = \begin{cases} \beta_2 \Delta t E_t [A]_t, & l \in [0, \Delta t); \\ [Y^{l-\Delta t}]_t, & l \in [\Delta t, \tau_2]; \\ 0, & l \in (\tau_2, \infty), \end{cases} \tag{23}$$

$$[AX^l]_{t+\Delta t} = \begin{cases} \beta_1 \Delta t [AA]_t + \beta_1 \Delta t ([X^{\tau_1}A]_t + [Y^{\tau_2}A]_t), & l \in [0, \Delta t); \\ [X^{\tau_1}X^{l-\Delta t}]_t + [Y^{\tau_2}X^{l-\Delta t}]_t + (1 - \beta_1 \Delta t - \beta_2 \Delta t E'_{x,t})[AX^{l-\Delta t}]_t, & l \in [\Delta t, \tau_1]; \\ 0, & l \in (\tau_1, \infty), \end{cases} \tag{24}$$

$$[AY^l]_{t+\Delta t} = \begin{cases} \beta_2 \Delta t E''_t [AA]_t + \beta_2 \Delta t E'_{y,t}[Y^{\tau_2}A]_t + \beta_2 \Delta t E'_{x,t}[X^{\tau_1}A]_t, & l \in [0, \Delta t); \\ [X^{\tau_1}Y^{l-\Delta t}]_t + [Y^{\tau_2}Y^{l-\Delta t}]_t + (1 - \beta_1 \Delta t - \beta_2 \Delta t E'_{y,t})[AY^{l-\Delta t}]_t, & l \in [\Delta t, \tau_2]; \\ 0, & l \in (\tau_2, \infty), \end{cases} \tag{25}$$

$$\begin{aligned} [AA]_{t+\Delta t} =&(1 - \beta_1 \Delta t - \beta_2 \Delta t E'_t)([X^{\tau_1}A]_t + [AX^{\tau_1}]_t + [Y^{\tau_2}A]_t + [AY^{\tau_2}]_t) \\ &+ ([X^{\tau_1}X^{\tau_1}]_t + [Y^{\tau_2}Y^{\tau_2}]_t + [X^{\tau_1}Y^{\tau_2}]_t + [Y^{\tau_2}X^{\tau_1}]_t) \\ &+ (1 - 2\beta_1 \Delta t - 2\beta_2 \Delta t E''_t)[AA]_t, \end{aligned} \tag{26}$$

$$[Y^{l_1}Y^{l_2}]_{t+\Delta t} = \begin{cases} 0, & l_1 \in [0, \Delta t) \text{ and } l_2 \in [0, \Delta t); \\ \beta_2 \Delta t E'_{y,t}[AY^{l_2-\Delta t}]_t, & l_1 \in [0, \Delta t) \text{ and } l_2 \in [\Delta t, \tau_2]; \\ \beta_2 \Delta t E'_{y,t}[Y^{l_1-\Delta t}A]_t, & l_2 \in [0, \Delta t) \text{ and } l_1 \in [\Delta t, \tau_2]; \\ [Y^{l_1-\Delta t}Y^{l_2-\Delta t}]_t, & l_1 \text{ and } l_2 \in [\Delta t, \tau_2]; \\ 0, & l_1 \text{ or } l_2 \in (\tau_2, \infty), \end{cases} \tag{27}$$

$$
[X^{l_1}X^{l_2}]_{t+\Delta t} = \begin{cases} 0, & l_1 \in [0, \Delta t) \ and \ l_2 \in [0, \Delta t); \\ \beta_1 \Delta t [AX^{l_2-\Delta t}]_t, & l_1 \in [0, \Delta t) \ and \ l_2 \in [\Delta t, \tau_1]; \\ \beta_1 \Delta t [X^{l_1-\Delta t}A]_t, & l_2 \in [0, \Delta t) \ and \ l_1 \in [\Delta t, \tau_1]; \\ [X^{l_1-\Delta t}X^{l_2-\Delta t}]_t, & l_1 \ and \ l_2 \in [\Delta t, \tau_1]; \\ 0, & l_1 \ or \ l_2 \in (\tau_1, \infty), \end{cases} \tag{28}
$$

$$
[X^{l_1}Y^{l_2}]_{t+\Delta t} = \begin{cases} 0, & l_1 \in [0, \Delta t) \ and \ l_2 \in [0, \Delta t); \\ \beta_1 \Delta t [AY^{l_2-\Delta t}]_t, & l_1 \in [0, \Delta t) \ and \ l_2 \in [\Delta t, \tau_2]; \\ \beta_2 \Delta t E'_{x,t} [X^{l_1-\Delta t}A]_t, & l_2 \in [0, \Delta t) \ and \ l_1 \in [\Delta t, \tau_1]; \\ [X^{l_1-\Delta t}Y^{l_2-\Delta t}]_t, & l_1 \in [\Delta t, \tau_1] \ and \ l_2 \in [\Delta t, \tau_2]; \\ 0, & l_1 \in (\tau_1, \infty) \ or \ l_2 \in (\tau_2, \infty), \end{cases} \tag{29}
$$

where

$$
E_t = \sum_{j=0}^{m} C_k^{k-j} \left(\frac{[AI]_t}{[A]_t} \right)^{k-j} \left(1 - \frac{[AI]_t}{[A]_t} \right)^j, \tag{30}
$$

$$
E'_{x,t} = \sum_{j=0}^{m} C_{k-1}^{k-1-j} \left(\frac{[IAX]_t}{[AX]_t} \right)^{k-1-j} \left(1 - \frac{[IAX]_t}{[AX]_t} \right)^j, \tag{31}
$$

$$
E'_{y,t} = \sum_{j=0}^{m} C_{k-1}^{k-1-j} \left(\frac{[IAY]_t}{[AY]_t} \right)^{k-1-j} \left(1 - \frac{[IAY]_t}{[AY]_t} \right)^j, \tag{32}
$$

and

$$
E''_t = \sum_{j=0}^{m-1} C_{k-1}^{k-1-j} \left(\frac{[IAA]_t}{[AA]_t} \right)^{k-1-j} \left(1 - \frac{[IAA]_t}{[AA]_t} \right)^j. \tag{33}
$$

In addition, we have

$$
[AX^l]_t = [X^l A]_t, \tag{34}
$$

$$
[AY^l]_t = [Y^l A]_t, \tag{35}
$$

$$
[X^{l_1}Y^{l_2}]_t = [Y^{l_2}X^{l_1}]_t, \tag{36}
$$

$$
[AI]_t = \sum_{l=0}^{\tau_1}[AX^l]_t + \sum_{l=0}^{\tau_2}[AY^l]_t, \tag{37}
$$

$$
[AI^l]_t = [AX^l]_t + [AY^l]_t. \tag{38}
$$

In the supplementary evolutionary equations of $[X^l]_{t+\Delta t}$, the fraction of X-type nodes with $l \in [0, \Delta t)$ at time $t + \Delta t$ is equal to the fraction of A-type nodes that fail due to internal causes in the time interval $[t, t+\Delta t)$. The fraction of X-type nodes with $\Delta t \leq l \leq \tau_1$ is equal to the fraction of X-type nodes with $\Delta t \leq l - \Delta t \leq \tau_1$ at time t. Since l cannot exceed the recovery time, the fraction of X-type nodes with $l > \tau_1$ is zero. The supplementary equations for $[Y^l]_{t+\Delta t}$ can be obtained in a similar way.

For the supplementary equations of $[AX^l]_{t+\Delta t}$, for $l \in [0, \Delta t)$, the first term means that the A-type neighbors of A-type nodes fail due to internal causes, which increases the fraction of AX^l edges with $l \in [0, \Delta t)$ at time $t + \Delta t$. The second (third) term depicts that the A-type nodes connected with an X-type (Y-type) neighbor fail due to internal causes while

15

their X-type (Y-type) neighbors recover spontaneously (i.e., recover because the recovery time has been reached), which increases the fraction of AX^l edges with $l \in [0, \Delta t)$. For $\Delta t \leq l \leq \tau_1$, the first (second) term describes that the X-type nodes connected with an X-type (Y-type) neighbor recover spontaneously, which increases the fraction of AX^l edges, with $l \in [\Delta t, \tau_1]$ at time $t + \Delta t$. The third term stipulates that there must be no change in the states of $AX^{l-\Delta t}$ edges, i.e., the A-type nodes associated with $AX^{l-\Delta t}$ edges have not failed during the time interval $[t, t + \Delta t)$. For $l > \tau_1$, we have $[AX^l]_{t+\Delta t} = 0$.

In the supplementary equation of $[AA]_{t+\Delta t}$, the first term denotes that, associated with edges $X^{\tau_1}A$, AX^{τ_1}, $Y^{\tau_2}A$ and AY^{τ_2}, the states of A-type nodes are not changed, but the states of the failed nodes have changed, which increases the fraction of AA edges at time $t+\Delta t$. The second term describes that both nodes at the end of $X^{\tau_1}X^{\tau_1}$, $Y^{\tau_2}Y^{\tau_2}$, $X^{\tau_1}Y^{\tau_2}$, and $Y^{\tau_2}X^{\tau_1}$ edges recover, which increases the fraction of AA edges. The third term stipulates that the states of both nodes at the end of AA edges must not change.

Similar to the MR model, we use E_t, E'_t, and E''_t to represent the probabilities that an active node satisfies the threshold condition $n \leq m$ in different cases.

Using the PA $[UVW]_t = [UV]_t[VW]_t/[V]_t$, we have

$$\frac{[IAX]_t}{[AX]_t} = \frac{[AI]_t}{[A]_t}, \tag{39}$$

$$\frac{[IAY]_t}{[AY]_t} = \frac{[AI]_t}{[A]_t} \tag{40}$$

and

$$\frac{[IAA]_t}{[AA]_t} = \frac{[AI]_t}{[A]_t}, \tag{41}$$

i.e., $E'_{x,t} = E'_{y,t}$. Letting $E'_{x,t} = E'_{y,t} = E'_t$, we have

$$E_t = \sum_{j=0}^{m} C_k^{k-j} \left(\frac{[AI]_t}{[A]_t}\right)^{k-j} \left(1 - \frac{[AI]_t}{[A]_t}\right)^j, \tag{42}$$

$$E'_t = \sum_{j=0}^{m} C_{k-1}^{k-1-j} \left(\frac{[AI]_t}{[A]_t}\right)^{k-1-j} \left(1 - \frac{[AI]_t}{[A]_t}\right)^j, \tag{43}$$

and

$$E''_t = \sum_{j=0}^{m-1} C_{k-1}^{k-1-j} \left(\frac{[AI]_t}{[A]_t}\right)^{k-1-j} \left(1 - \frac{[AI]_t}{[A]_t}\right)^j. \tag{44}$$

The number of supplementary equations depends on the time step Δt. If Δt is small compared with other time scales in the dynamics, the number of supplementary equations will be large.

3. Relationship between MR and NMR models

For the MR model, the supplementary mean-field equations can be written concisely as

$$\begin{cases} \dfrac{d[X]_t}{dt} = \beta_1[A]_t - \mu_1[X]_t, \\ \dfrac{d[Y]_t}{dt} = \beta_2 E_t[A]_t - \mu_2[Y]_t, \end{cases} \tag{45}$$

where

$$E_t = \sum_{j=0}^{m} C_k^{k-j}([I]_t)^{k-j}(1 - [I]_t)^j. \tag{46}$$

For the NMR model, in a compact form, the supplementary mean-field equations are

$$\begin{cases} [X]_{t+\Delta t} = \beta_1 \Delta t[A]_t + [X]_t - [X^{\tau_1}]_t, \\ [Y]_{t+\Delta t} = \beta_2 \Delta t E_t[A]_t + [Y]_t - [Y^{\tau_2}]_t, \end{cases} \tag{47}$$

where

$$E_t = \sum_{j=0}^{m} C_k^{k-j}([I]_t)^{k-j}(1 - [I]_t)^j. \tag{48}$$

When the system has reached a steady state $(t \to \infty)$, we have $[\dot{A}]_t = 0$, $[\dot{X}]_t = 0$ and $[\dot{Y}]_t = 0$. Supplementary Eq. (47) can be written as

$$\begin{cases} \beta_1[A]_t - [X^{\tau_1}]_t = 0, \\ \beta_2 E_t[A]_t - [Y^{\tau_2}]_t = 0. \end{cases} \tag{49}$$

From Supplementary Eq. (49), we have

$$[X^{\tau_1}]_t = \beta_1[A]_t = C_1 \tag{50}$$

and

$$[Y^{\tau_2}]_t = \beta_2 E[A]_t = C_2, \tag{51}$$

where C_1 and C_2 are constants. In addition, we have

$$[X^l]_t = [X^{\tau_1}]_{t+\tau_1-l} = C_1 \tag{52}$$

and

$$[Y^l]_t = [Y^{\tau_2}]_{t+\tau_2-l} = C_2. \tag{53}$$

We then have

$$[X]_t = \Sigma_l^{\tau_1}[X^l]_t = \tau_1[X^{\tau_1}]_t, \tag{54}$$

which gives

$$[X^{\tau_1}]_t = \frac{1}{\tau_1}[X]_t. \tag{55}$$

Similarly, we can get

$$[Y^{\tau_2}]_t = \frac{1}{\tau_2}[Y]_t. \tag{56}$$

Supplementary Equation (49) can then be rewritten as

$$\begin{cases} \beta_1 [A]_t - \dfrac{1}{\tau_1} [X]_t = 0, \\ \beta_2 E_t [A]_t - \dfrac{1}{\tau_2} [Y]_t = 0. \end{cases} \tag{57}$$

Comparing with the steady-state solution of the MR model:

$$\begin{cases} \beta_1 [A]_t - \mu_1 [X]_t = 0, \\ \beta_2 E_t [A]_t - \mu_2 [Y]_t = 0, \end{cases} \tag{58}$$

we see that the steady states for both models are equivalent to each other for fixed values of $\mu_1 = 1/\tau_1$ and $\mu_2 = 1/\tau_2$.

B. Supplementary Note 2: Effects of different initial conditions on failure propagation and evolutionary trajectories of failed nodes

Supplementary Figs. 1 and 2 illustrate the effects of initial conditions on failure propagation dynamics. The different recovery mechanisms make the competition processes between the X-type and Y-type nodes distinct for the MR and NMR models. In general, non-Markovian features render more complicated the failure-recovery dynamics. Here we investigate how the fraction of initially failed nodes $[I]_0$ influences the phase transition in the NMR model.

We set the initial conditions as $[X]_0 \neq 0$ and $[Y]_0 = 0$. When the fraction of initially failed nodes is sufficiently small, e.g., $[X]_0 = 0.05$, as in Supplementary Fig. 3(a), active nodes fail most likely because of internal causes. In both MR and NMR models, the system will evolve into a low-failure state (phase), where the trajectories evolve from t_O to t_A. As $[X]_0$ increases to 0.2, as shown in Supplementary Fig. 3(d), the evolutionary process for the MR model is similar to the case in Supplementary Fig. 3(a): the trajectory evolves from t_O to t_A. This is because the X-type nodes not only are born at the rate β_1 but also recover at the rate μ_1, driving the system to a dynamic equilibrium associated with the low-failure phase. As a result, there are insufficient newly created X-type nodes to cause a large scale external failure. In contrast, in the NMR model, X-type nodes are always created but, in the early stage $[t_O, t_A]$, there is no recovery because of the memory effect. Once the fraction of failed nodes, including the initial and the newly created X-type nodes in $[t_O, t_A]$, reaches a critical value determined by the criterion that many A-type nodes with active neighbors satisfy the threshold condition $n_A \leq m$, $[Y]$ increases rapidly and the trajectory moves from t_A to $t_{A'}$. In the time interval $[t_{A'}, t_{B'}]$, $[Y]$ decreases slowly due to a short recovery time $\tau_2 = 1$, while internal failures make $[X]$ increase slowly because $t_{B'} < 100$. In the time interval $t \in [100, 100 + \Delta t)$, the age of the initially failed nodes ($[I]_0 = [X]_0 = 0.2$) reaches the recovery time and these nodes will turn into A state simultaneously. Consequently, $[X]$ decreases suddenly to a low value and the trajectory evolves sharply from $t_{B'}$ to $t_{C'}$. At this time, $[I]$ still remains at a high value, making more active nodes (including the original and new X-type nodes) satisfy the threshold condition $n_A \leq m$ and resulting in a rapid growth of Y-type nodes in the time interval $[t_{C'}, t_{D'}]$. At time $t_{D'}$, $[I]$ increases to a higher

18

value, rendering more competitive Y than X state as they compete for A-type nodes. As a result, A-type nodes fail due mostly to external causes, and $[Y]$ ($[X]$) continues to increase (decrease) in the time interval $[t_{D'}, t_{E'}]$.

For $[X]_0 = 0.3$, as shown in Supplementary Fig. 3(g), the evolutionary process of the MR model is consistent with that in Supplementary Fig. 3(d). For the NMR model, the evolutionary process is different from that in Supplementary Fig. 3(b). In the time interval $[t_{B'}, t_{C'}]$, more initially failed nodes with $[I]_0 = [X]_0 = 0.3$ recover simultaneously because their age (i.e., the current time) has reached the recovery time $\tau_1 = 100$. At time $t_{C'}$, a relatively low value of $[I]$ makes fewer active nodes satisfy the threshold condition $n_A \leq m$. Because of the short recovery time, all the current Y-type nodes switch into the active state in the time interval $[t_{C'}, t_{D'}]$. After that, many active nodes fail internally and become X-type nodes, so $[X]$ increases continuously and the trajectory moves from $t_{D'}$ to t_A.

When the initial value $[X]_0$ is sufficiently large, e.g., 0.6 as in Supplementary Fig. 3(j), many A-type nodes will fail due to external causes and $[Y]$ will increase rapidly in both models, as shown in the trajectory from t_O to t_A. After that, in the MR model, the increment of $[Y]$ enhances the probability for active nodes to switch into the Y state, while increasingly X-type nodes recover and turn to the A state. The corresponding trajectory moves from t_A to t_B. In the NMR model, the evolutionary process is similar to that in Supplementary Fig. 3(g).

C. Supplementary Note 3: Markovian and non-Markovian dynamics when external recovery is slower than internal recovery

In the main text, the case where internal recovery is slower than external recovery, i.e., $\tau_1 > \tau_2$, is treated. There are situations in the real world where the opposite, i.e., $\tau_1 < \tau_2$, can occur. For example, in the case of an earthquake, the recovery of a node in an infrastructure (e.g., restoring a damaged building) may require more time than that of repair due to internal material failures. To study this case, we fix the network topology as in Supplementary Fig. 1. Supplementary Fig. 4 shows the representative results. Comparing Supplementary Fig. 4(a) with Fig. 2(b) in main text, we see that they demonstrate qualitatively similar behaviors, indicating the applicability of our theoretical framework for the case $\tau_1 < \tau_2$.

Supplementary Fig. 5 shows the phase diagram on the initial-condition plane ($[X]_0, [Y]_0$). Comparing it with Fig. 7 in the main text, we see that both exhibit similar phenomena, although the quantitative details are different. This further validates that our developed framework is applicable to the case $\tau_1 < \tau_2$.

D. Supplementary Note 4: Effects of network structure on Markovian and non-Markovian recovery dynamics

In general, network topology can have a significant effect on the cascading process of failure propagation. In the main text, we have discussed two kinds of network topology, i.e., random regular and scale-free networks, and found that memory in the nodal recovery can counterintuitively make both types of networks more resilient against large scale failures. Here we study two additional types of network: those with degree-degree correlation and a

community structure, respectively, and demonstrate the same effect of memory.

1. Effects of degree-degree correlation

To generate networks with adjustable degree-degree correlation coefficients, we use the standard edge-rewiring procedure [1, 2]. In particular, we first generate an uncorrelated configuration network (UCN) [3] with the degree range $[k_{\min}, \sqrt{N}]$ and degree distribution $P(k) \sim k^{-\gamma}$. Keeping the degree of each node unchanged, we adjust the degree-degree correlation through the following process. Firstly, at each step, we randomly choose two edges in the network, disconnect them, and switch the two links among the four chosen nodes. Secondly, to generate an assortative (a disassortative) network, we add a new edge between the highest degree and the second highest (lowest) nodes and then connect the remaining pair of nodes. If either of the new edges already exists, we leave the network unchanged. Thirdly, we repeat the process until the observed degree-degree correlation coefficient has reached a target value, which is defined as [4]:

$$r = \frac{\sum_{ij}(A_{ij} - k_i k_j/2m_{\rm e})k_i k_j}{\sum_{ij}(k_i \delta_{ij} - k_i k_j/2m_{\rm e})k_i k_j},\tag{59}$$

where $m_{\rm e}$ is the total number of edges in the network, $A_{ij} = 1$ if there is an edge between the node i and j (otherwise, $A_{ij} = 0$), δ_{ij} is the Kronecker delta (1 if $i = j$ and 0 otherwise). There is no degree-degree correlation for $r = 0$, but the network will have positive (negative) degree-degree correlation for $r > 0$ ($r < 0$).

Supplementary Figs. 6(a-d) show the degree-degree correlation properties of the UCNs for $r = 0$, $r = 0.5$, $r = 0.7$ and $r = -0.5$, respectively, where it can be visually seen that the high-degree nodes in the network with a positive correlation tend to be connected together, while a high-degree node in the case of negative correlation tends to be connected to a low-degree one. Supplementary Fig. 7 shows the probability distribution of one node of degree k_i connecting to another node of degree k_j, where panels (a-d) correspond to the cases of $k_i = 5$, $k_i = 20$, $k_i = 40$ and $k_i = 60$, respectively.

Supplementary Fig. 8 shows the results of spontaneous recovery dynamics on UCNs with different levels of degree-degree correlation for $N = 10000$, $k_{\min} = 5$, and $k_{\max} = 100$. Supplementary Figs. 8(a) and 8(c) show the dependence of $[I]$ on adiabatic variations in β_1 in the steady state for the MR and NMR models, respectively. The blue circles, orange down triangles, green up triangles and red squares are the average simulation results for degree-degree correlation coefficient $r = 0$, $r = 0.5$, $r = 0.7$ and $r = -0.5$, respectively, where the system is regarded as in the low-failure phase when β_1 is smaller than the critical value $\beta_{\rm c}$ and a large scale failure occurs when β_1 exceeds $\beta_{\rm c}$. For the case of zero degree-degree correlation, the network can remain in the low-failure phase for the largest possible value of $\beta_{\rm c}$, indicating the highest possible degree of resilience. However, in the high-failure phase with adiabatically decreasing value of β_1, the network with a high level of degree-degree correlation has a larger value of $\beta_{\rm c}$, signifying a stronger ability to recover from damage. As a result, in spontaneous recovery models, UCNs with degree-degree correlations can make the hysteresis region smaller, regardless of positive or negative degree-degree correlation. Supplementary Figs. 8(b) and 8(d) present further evidence to support the finding in the

main text that non-Markovian recovery makes the networks more resilient against large scale failures, regardless of the detailed network structure.

To explain why positive or negative degree-degree correlation shrinks the hysteresis region in Fig. 8, we focus on the MR model. Supplementary Fig. 9(a) shows the time evolution of the fraction of Y-type nodes for $\beta_1 = 0.004$ and $[X]_0 = 0.2$, where the the system is in the low-failure phase. The degree correlation tends to reduce the resilience of system, thereby promoting cascading failures. Corresponding to the steady-state of $[I]$ in Supplementary Fig. 8(a), we see that the large scale failure results from the sharp increase of $[Y]$. Supplementary Figs. 9(b) and 9(c) show the evolution of the mean degree of the newly emerged Y-type nodes and the standard variance of the nodal degree, respectively. It can be seen that, for the networks with $r = 0.7$ (-0.5), the degree values of many newly emerged Y-type nodes are similar for $t < 650$ ($t < 470$). However, after that, the degrees of newly emerged node vary. While the results of both cases look similar, the underlying topological properties of the network are different. In particular, in scale-free networks with a highly heterogeneous degree distribution, a large proportion of the nodes have smaller degrees than the mean degree, but a few hubs have larger degrees. For an assortative network, nodes of similar degree are more likely to be connected together. As a result, there are more vulnerable nodes of low degrees connecting to each other [e.g., the nodes with $k_i = 5$ as shown in Supplementary Fig. 7(a)], which comprise a sizable vulnerable component, making the network more susceptible to a large scale failure [5]. When the threshold on external failure (i.e., the critical fraction of the active neighbors) is fixed (e.g., 0.5), a low-degree node is vulnerable because it is more easily affected by its neighboring nodes. For a disassortative network, the high-degree nodes prefer to connect to the vulnerable nodes of low degrees [e.g., the nodes of $k_i = 20$ shown in Supplementary Fig. 7(b)], making the hubs more vulnerable against the failures of their neighboring nodes and promoting cascading failures.

Supplementary Fig. 9(d) shows the time evolution of $[Y]_t$ for the MR model for $\beta_1 = 0.0022$ and $[X]_0 = 0.6$, corresponding to the case where the degree correlation suppresses the occurrence of cascading failure when the system is in the high-failure phase. From Supplementary Figs. 9(d-f), we see that for the cases of $r = 0.7$ and $r = -0.5$, there are a large number of externally failed nodes of various degrees in the transient process, after which the system undergoes a sharp decrease in $[Y]_t$ near $t = 250$ and $t = 570$, respectively, leaving few externally failed nodes with a similar degree. The reason that the fraction of $[Y]_t$ decreases sharply is also the vulnerable components. For a small value of β_1, the recovery of a few vulnerable nodes will cause successive recovery of the other connected vulnerable nodes and eventually block failure propagation. Note that, for $r = 0$, the high-failure phase continues, because a more stable high-failure phase depends on the structure in which nodes of quite distinct degrees are connected together, as verified by the results in Supplementary Figs. 6 and 9(f).

2.   Effects of community structure

For simplicity, we consider networks that contain two two communities [6, 7], where each community is composed of n nodes and so the network size is $N = 2n$. Nodes in the same community are connected to each other with the probability p_{in}, while links across the two communities occur with the probability p_{out}, so the ratio of the numbers of edges in and

21

between the communities is $\eta \approx p_{\text{in}}/p_{\text{out}}$. The degree distributions of the subnetwork in each community and of the whole network are Poisson. Note that the value of η determines the strength of the community structure. In particular, $\eta = 1.0$ means that the numbers of edges in and between communities are the same so, effectively, there is no community structure. Likewise, a value of η much greater than one indicates a stronger community structure with significantly more edges within the individual communities. Quantitatively, the community strength can be measured by the modularity Q defined as [4]

$$Q = \frac{1}{2m_{\text{e}}}\sum_{ij}(A_{ij} - \frac{k_i k_j}{2m_{\text{e}}})\delta(c_i, c_j), \tag{60}$$

where m_{e} is the total number of edges in the network, A_{ij} are the elements of the network adjacency matrix, c_i is the community to which node i belongs, and δ_{ij} denotes the Kronecker delta. The value of Q is strictly less than 1.0, where $Q > 0$ ($Q < 0$) means that there are more (less) edges between nodes in the same communities than can be expected by chance.

In our numerical simulations, we fix $N = 3000$ and mean degree $\langle k \rangle = 6$, and generate three typical networks with $\eta = 1.0$, 15.0 and 30.0, with the corresponding approximate Q values -0.01, 0.43 and 0.46, respectively. Initially, we randomly distribute seeds in the whole network. Supplementary Fig. 10 demonstrates the dynamical behaviors for both the MR and NMR models. It can be seen that, if the system is in a low-failure (high-failure) phase, the community structure tends to reduce (enhance) resilience. The reason is that nodes in the same community tend to be connected more closely and thus constitute a high clustering structure. The failure of a node due to an external mechanism tends to enhance the probability for other nodes in the same community to fail. Similarly, if a node has recovered, the probability for other nodes in the same community to recover is increased. As a result, when the system is in the low failure phase, the community structure makes a large scale failure more likely. In contrast, if the system is in the high failure phase, the community structure can facilitate recovery. Qualitatively, these results are consistent with those in Supplementary Note 4.

E.   Supplementary Note 5: Markovian and non-Markovian recovery dynamics in empirical networks

We study Markovian and non-Markovian recovery dynamics in empirical networks, using the arenas-email and the friendship-hamster networks as two examples, where the former is an email communication network [8] of size $N = 1133$ and average degree $\langle k \rangle = 9.6$, and the latter is the network of friendship among the users of the website hamsterster.com [9] with $N = 1858$ and $\langle k \rangle = 13.4$. Simulation results reveal the same phenomenon as in other cases, i.e., non-Markovian type of recovery with a memory tends to enhance the network resilience against large scale failures, as shown in Supplementary Fig. 11.

F. Supplementary Note 6: Markovian and non-Markovian recovery dynamics in power-grid synchronization

An idealized model for a power grid is the network of Kuramoto oscillators, where the weighted coupling coefficient between two oscillators is related to their own natural frequencies [10, 11]. We study the following model [12]:

$$\frac{d\theta_i}{dt} = \omega_i + \frac{\lambda|\omega_i|}{k_i} \sum_{j=1}^{N} A_{ij} \sin(\theta_j - \theta_i), \quad i = 1, \dots, N , \tag{61}$$

where ω_i is the natural frequency of oscillator i randomly chosen from the Lorentzian distribution

$$g(\omega) = \frac{1}{\pi}\left[\frac{\Delta}{(\omega - \omega_0)^2 + \Delta^2}\right], \tag{62}$$

λ is the overall coupling strength, $k_i = \sum_{j=1}^{N} A_{ij}$ is the degree of node i, and A_{ij} are the elements of the symmetric adjacency matrix. In this model, explosive synchronization [12, 13] can arise. In the regime of complete synchronization, all oscillators are localized in the same area. To investigate the propagation of synchronization under the MR and NMR dynamics, we fix the synchronization area and construct the following dynamical system of phase oscillators:

$$\frac{d\theta_i}{dt} = \omega_i + \frac{\lambda|\omega_i|}{k_i} \sum_{j=1}^{N} A_{ij} \sin(\theta_j - \theta_i) - a \sin(\theta_i - \phi), \quad i = 1, \dots, N , \tag{63}$$

where a is a parameter characterizing the degree of synchronization. The first and third terms on the right-hand side describe the self-dynamics of node i, while the second term represents the interactions between node i and its interacting partners. To see the meaning of ϕ, we introduce the order parameter R

$$Re^{i\Psi} = \frac{1}{N} \sum_{j=1}^{N} e^{i\theta_j}, \tag{64}$$

where $0 \leq R \leq 1$ and Ψ denotes the average phase. The synchronization region can then be defined as $[\phi - \psi, \phi + \psi]$. For the MR dynamics, each oscillator in the synchronized region has the probability p to return to the asynchronous state with a random phase between $[-\pi, \pi]$. For the NMR process, each oscillator can stay in the synchronized region for time $\tau = 1/p$ before leaving the region to become asynchronous with others.

We carry out synchronization simulations on a completely connected network (CN) and a random regular network (RRN) with average degree $\langle k \rangle = 10$. We find that, for both networks, the system transitions to the high-failure (low-failure) phase when increasing (decreasing) λ towards a critical value λ_c. Supplementary Fig. 12 shows the dynamic behaviors for both the MR (orange squares) and NMR (blue circles) dynamics. It can be seen that the results are qualitatively similar to those in either Supplementary Fig. 10 or Supplementary Fig. 11, indicating that non-Markovian recovery makes the network more resilient against large scale breakdown of synchronization. The results also indicate that the network topology can have a considerable impact on the system resilience.

III. SUPPLEMENTARY REFERENCES

[1] Xulvi-Brunet, R. & Sokolov, I. M. Reshuffling scale-free networks: From random to assortative. *Phys. Rev. E* **70**, 066102 (2004).

[2] Gao, L., Wang, W., Pan, L., Tang, M. & Zhang, H.-F. Effective information spreading based on local information in correlated networks. *Sci. Rep.* **6**, 38220 (2016).

[3] Catanzaro, M., Boguná, M. & Pastor-Satorras, R. Generation of uncorrelated random scale-free networks. *Phys. Rev. E* **71**, 027103 (2005).

[4] Newman, M. *Networks* (Oxford University Press, 2010).

[5] Payne, J. L., Dodds, P. S. & Eppstein, M. J. Information cascades on degree-correlated random networks. *Phys. Rev. E* **80**, 026125 (2009).

[6] Girvan, M. & Newman, M. E. Community structure in social and biological networks. *Proc. Natl. Acad. Sci. (USA)* **99**, 7821–7826 (2002).

[7] Condon, A. & Karp, R. M. Algorithms for graph partitioning on the planted partition model. *Random Stru. Algo.* **18**, 116–140 (2001).

[8] U. Rovira i Virgili network dataset – KONECT (2017). URL `http://konect.cc/networks/arenas-email`.

[9] Hamsterster friendships network dataset – KONECT (2017). URL `http://konect.cc/networks/petster-friendships-hamster`.

[10] Dorfler, F. & Bullo, F. Synchronization and transient stability in power networks and nonuniform Kuramoto oscillators. *SIAM J. Cont. Opt.* **50**, 1616–1642 (2012).

[11] Wang, H. & Li, X. Synchronization and chimera states of frequency-weighted Kuramoto-oscillator networks. *Phys. Rev. E* **83**, 066214 (2011).

[12] Zhang, X., Hu, X., Kurths, J. & Liu, Z. Explosive synchronization in a general complex network. *Phys. Rev. E* **88**, 010802 (2013).

[13] Hu, X. *et al.* Exact solution for first-order synchronization transition in a generalized kuramoto model. *Sci. Rep.* **4**, 7262 (2014).